University of California
Los Angeles

Image inpainting using a modified Cahn-Hilliard equation

A dissertation submitted in partial satisfaction
of the requirements for the degree
Doctor of Philosophy in Mathematics

by

Alan Gillette

2006

The dissertation of Alan Gillette is approved.

Alan Yuille

Luminita Vese

Stanley Osher

Andrea Bertozzi, Committee Chair

University of California, Los Angeles

2006

Dedicated to my wife Brooke, who put up with the long hours,
and to my parents, who were always there to help.

Table of Contents

1 Introduction **1**

1.1 The origins of inpainting 1

1.2 Automated inpainting prior to 2000 2

1.3 Partial differential equation based inpainting: 2000-2006 3

1.4 Origins of the Cahn-Hilliard equation 11

1.5 Solutions of the Cahn-Hilliard equation 16

2 Analysis **18**

2.1 Proposed model 18

2.2 Global existence of weak solutions of the modified Cahn-Hilliard equation 21

2.3 Fidelity and boundary conditions 25

2.3.1 Key estimates 26

2.3.2 Matching isophotes as λ_0 becomes large 31

2.4 Matching of isophotes for binary images: continuity of the edge direction 34

2.5 Bifurcations of the modified Cahn-Hilliard equation 38

3 Numerical Algorithm **44**

3.1 Convexity splitting algorithm for the modified Cahn-Hilliard equation 45

3.2 Fourier spectral method used for computation 46

4 Results 51

4.1 Inpainting of a double stripe 51

4.2 Inpainting of a cross 52

4.3 Inpainting across large gaps 53

4.4 Inpainting of a sine wave 53

4.5 Inpainting of a road 55

4.6 Recovery of text 58

4.7 Super-resolution 59

4.8 Comparison with other methods 60

4.9 Graphic results 61

5 Future Projects 64

5.1 Grayscale inpainting using the modified Cahn-Hilliard equation . 64

6 Conclusion 69

References 70

List of Figures

1.1 Image from [She03]. Inpainting problem solved by using the Mumford-Shah inpainting technique, shown as an example. Note that the isophotes are not smoothly continued at the boundary of the inpainting region. 11

1.2 Image from [BSC00]. Inpainting problem solved by using the method described in [BSC00] by Bertalmio et. al. 12

2.1 Inpainting problem. The isophote vectors are shown. 32

2.2 (a) Gray portion denotes the inpainting region D while the black and white portion denote the background image f. (b) Steady state solution of (2.35) showing a completed stripe. (c) Steady state solution of (5.7) showing a broken stripe. In both cases $\varepsilon = 0.01$. In all cases we choose a square of 128×128 grid points, with the inpainting region having a gap of width 40 grid points. The grid spacing is $\Delta x = 0.01$. 39

2.3 Bifurcation diagrams for, (a) gap of 30, (b) gap of 45, (c) gap of 80. The y-axis shows the steady state height of the midpoint of the stripe, while the x-axis is the epsilon value. The steady states are shown visually in thumbnails, with an arrow pointing to their positions on the respective bifurcation diagrams. Only stable steady states are shown. 40

2.4 Bifurcation diagrams relating to the phenomena shown in figure 2.3. (a) An incomplete pitchfork bifurcation. (b) A symmetric pitchfork bifurcation. (c) Another incomplete pitchfork bifurcation. 41

2.5 Disconnected stripe with a gap of 20, at (a) t=0, (b) t=299, after steady state had been reached for $\varepsilon = .8$, (c) t=500 (produced by switching to $\varepsilon = .01$ at t = 300). 43

4.1 (a) Initial data (inpainting region in gray). (b) Intermediate state at $t = 50$. (c) steady state at $t = 700$. (Gap distance is 30 units, Image domain is 128×128). 52

4.2 (a) Initial data of cross (inpainting region in gray). (b) Intermediate state at $t = 300$. (c) Steady state at $t = 1000$. (Image domain is 128×128, stripe width is 20 units, initial gap distance is 50 units). . . 52

4.3 (a) Initial data (inpainting region in gray). (b) Intermediate state at $t = 499$. (c) near steady state at $t = 8000$. (Gap distance is 100 units, and the stripe width is 5 units. Image domain is 128×128.) 53

4.4 Inpainting a sine wave. (Image domain is 128×128). 54

4.5 Inpainting of an obscured road. (Image domain is 128×128). 55

4.6 Recovery of damaged text. (Image domain was 128×128). 57

4.7 Recovery of damaged text. (Image domain was 256×256). 57

4.8 Recovering obscured text. (Image domain is 256×256). 58

4.9 Super-resolution of text. Magnification 3X. (Original size 64×64). . . 59

4.10 Inpainting data for comparison tests. Gray color denotes inpainting regions. 61

4.11 Results for the circle inpainting test. [1] – zero initial data assumed in inpainting region. [2] – random initial data assumed in inpainting region. 61

4.12 Results for the stripe inpainting test. [1] – zero initial data assumed in inpainting region. [2] – random initial data assumed in inpainting region. 62

5.1 A multi-welled $W(u)$ with numerous zeros between $x = 0$ and $x = 1$. 65

5.2 A result showing how the modified Cahn-Hilliard with the addtion of a multi-welled $W(u)$ performed. 65

List of Tables

4.1 Comparison tests, inpainting region set to zero data 63

4.2 Comparison tests, inpainting region set to random data 63

Acknowledgments

I would like to thank everyone involved in helping me achieve my goal of completing the Ph.D. degree program at UCLA.

Foremost, thanks goes to my advisor, Dr. Andrea Bertozzi for her wise guidance throughout my time as a graduate researcher. Her energy and clarity of focus provided invaluable help in reaching closure on this thesis topic. Also appreciated were her efforts to ensure my successful transition from graduate school to post-graduate work.

I would like to thank Dr. Selim Esedoglu for his patient help in getting me started with the research on image inpainting using the Cahn-Hilliard equation. His knowledge of analysis and numerics was always very helpful and inspiring.

Thanks goes to Dr. Steven Krantz at Washington University, for his kind recommendation of me to the UCLA Mathematics program. This recommendation came almost 10 years after I had been in his class, so his taking the time to write on my behalf is very much appreciated. I also appreciate the fact that he gave me his book on problem solving (which was on his desk), simply because I expressed interest in it!

As well, I would like to thank the following people for their kind recommendations to graduate school: Dr. John Scandrett of Washington University Physics, Dr. Ronald Friewald of Washington University, Mr. Karl Wolf of St. Louis, and Mr. Steve Datnow of Sausalito. All of these people had to take time away from busy schedules to write 7 different recommendations and evaluations. I remain in their debt.

I would like to thank my parents, Willard and Mary-Lou Gillette of Fremont, California, for their patience and kind support (both emotional and financial) during my time in graduate school. Mom and Dad – you're cheerleading really helped, and I will always remember it!

Finally, I am very grateful to have an incredibly supportive wife, Brooke Gillette. Without her kindness and support, graduate school would have been a very lonely experience. Instead, it was a joy. Brooke – I love you, you're the best.

This work was supported by the National Science Foundation and the intelligence community through the joint "Approaches to Combat Terrorism" program (NSF Grant AST-0442037), and as well by ONR grant N000140410078 and NSF grants CCF-0321917 and DMS-0410085.

VITA

1969	Born, North Andover, Massachusetts
1988 - 1992	B.A.
	Washington University, St. Louis, MO
2001 - 2006	Ph.D
	UCLA, Los Angeles, California

Abstract of the Dissertation

Image inpainting using a modified Cahn-Hilliard equation

by

Alan Gillette

Doctor of Philosophy in Mathematics

University of California, Los Angeles, 2006

Professor Andrea Bertozzi, Chair

Image inpainting is the process of filling in missing parts of damaged images based on information gleaned from surrounding areas. We propose a model for inpainting binary images using a modified Cahn-Hilliard equation, and develop very efficient numerical techniques for its solution. The Cahn-Hilliard equation is fourth order, and nicely allows for isophote directions to be matched at the boundary of inpainting regions. Our model has two scales, the diffuse interface scale, ε, on which it can accomplish topological transitions, and the feature scale of the image.

We show via simulations that a dynamic two step method involving the diffuse interface scale allows us to connect regions across large inpainting domains. For the model problem of stripe inpainting, we show that this issue is related to a bifurcation structure with respect to the diffuse interface scale ε. Future directions for this model will account for grayscale inpainting, and may incorporate wavelet methods.

CHAPTER 1

Introduction

1.1 The origins of inpainting

The story of inpainting begins in the art world. For centuries, people have been keenly interested in repairing missing sections of oil paintings, and doing so in a way that renders the restoration as imperceptible as possible. However, differences of opinion regarding the best way to accomplish the retouching have been present from art restoration's inception.

Inpainting of artworks began as early as the Renaissance. Much of the existing artwork for this period came from the Roman era, and was badly in need of repair. These crucifixions and sundry religious scenes were restored by 14th century artists who softened the Roman style to their own tastes, often inpainting blue skies in a blank region where a gold coloring had previously lay.

But by no means were these Renaissance artists exceptional in their decision to use tastes from their own era in the restoration of art from earlier periods. In fact, this was to become the rule, as each generation had its own viewing public it was held accountable to, and as well, its own mechanical advances that it wished to employ. In this way, art restoration has always remained dependent on popular thought and economic concerns (for an excellent introduction to the history of painting restoration and its problems, please see [Wal04]).

By the 20th century, many art restorers began to suggest that large missing portions of an image should be inpainted with a "neutral" tone. In practice, the immediate problem was that few could agree what "neutral" tone was, and how context changed its definition. It soon became clear that even the most carefully chosen flat tone for a damaged region could exhibit magnet-like behavior with respect to the eye of the viewer, calling attention to the very problem it hoped to disguise.

However, in a more recent adaptation of this method, damaged regions of paintings have been inpainted with a delicate construction of fine, parallel lines of a single color. Done in the appropriate manner, this method seems to add a component to the texture of a region that makes the inpainting believable to an untrained eye, even from only a few yards away.

For the art restorer, this discussion has touched upon only a minute portion of the spectrum of concerns that must go into the repair of a painting. For the mathematician, however, it gives us clear insight to the truth that there is no one "best" way to perform inpainting.

1.2 Automated inpainting prior to 2000

Starting in the 1980s, a few general methods for inpainting came into wide use. Stochastic inpainting methods used statistics generated by portions of the existing image to find probabilities of what should exist in the missing inpainting regions. Examples of this are simulated annealing and neural net inpainting schemes, among others. Other methods focussed on edge detection and scale-space filtering. The chief example of this in the years prior to 2000 is anisotropic diffusion.

In 1984, Geman and Geman [GG84] used simulated annealing to accomplish inpainting tasks. The simulated annealing algorithm provides a way to search for a fairly good minimum value of a cost function, when finding a precise global minimum may be extremely difficult. An excellent introduction to simulated annealing can be found in Kirkpatrick, Gellatt, and Vecchi [KJV82]. Geman and Geman used a statistical cost function that, when used in conjunction with simulated annealing, maximized the most probable state of the image under a Gibbs distribution.

In 1992, Perona and Malik [PM90] introduced the idea of anisotropic diffusion to inpainting. They showed that this method could be seen as a gradient descent on an energy, and that it could be applied to multiscale image segmentation. The important point was that they found a way to encourage intra-region smoothing in preference to interregion smoothing [PM90]. That is, sharp edges were left mostly intact by their algorithm.

It should be noted that the scale-space filtering that Perona and Malik used built upon earlier work by Rosenfeld and Thurston [RT71], as well as Yuille and Poggio [YP86], among others.

1.3 Partial differential equation based inpainting: 2000-2006

The work of Bertalmio et. al. [BSC00] introduced image inpainting as a new research area of digital image processing. Their model is based on nonlinear partial differential equations, and is designed to imitate the techniques of museum artists who specialize in restoration. In particular, Bertalmio et. al. elucidated the principle that good inpainting algorithms should propagate sharp edges in surrounding areas into the damaged parts that need to be filled in. This can be done for instance by connecting contours of constant grayscale image intensity (called isophotes) to each other across the inpainting region, so that gray levels at the edge of the the damaged region get extended to the interior continuously. They also imposed the direction of isophotes as a boundary condition at the edge of the inpainting domain.

The isophote direction is defined as

$$\nabla^{\perp}u(x,y) = (-\frac{\partial}{\partial y}, \frac{\partial}{\partial x})u(x,y), \tag{1.1}$$

where $u(x, y)$ is the image data (grayscale value) at a point (x, y) in the two-dimensional picture. Image data from the boundary of the inpainting region is then propagated a short distance into the inpainting region along these isophotes.

The PDE to solve is then

$$\frac{\partial u}{\partial t} + \nabla^{\perp}u \cdot \nabla\Delta u = 0. \tag{1.2}$$

This has the effect of propagating the smoothness operator Δu into the inpainting region. Every few steps in the numerical process, an iteration of anisotropic diffusion is added by calculating

$$\frac{\partial u}{\partial t} = \kappa(x,y,t)|\nabla u(x,y,t)|$$

at all points within the inpainting region. Here, $\kappa(x, y, t)$ is the curvature of the two-dimensional surface $u(x, y, t)$ at the point (x, y). This diffusion process allows the successive isophote lines to curve, if need be, as they are propagated.

In subsequent work with Bertozzi [BBS01], they realized that the nonlinear PDE introduced in [BSC00] has intimate connections with two dimensional fluid dynamics the Navier-Stokes equations. Indeed, it turns out that the steady state problem originally proposed in [BSC00] is equivalent to the inviscid Euler equations from incompressible flow, in which the image intensity function plays the role of the stream function in the fluid problem.

If $u(x, y, t)$ is taken as the grayscale value at a point in the image, then

$$\begin{aligned} \Delta u &= w, \qquad u|_{\partial D} = u_0, \\ v &= \nabla^{\perp} u, \end{aligned}$$

and the smoothness estimator is evolved according to

$$\frac{\partial w}{\partial t} + v \cdot \nabla w = \nu \nabla \cdot \Big[g(|\nabla w|) \nabla w \Big], \tag{1.3}$$

where ν is a constant, and $g(|\nabla w|)$ allows for anisotropic diffusion of $u(x, y, t)$ within the inpainting region only. (Note – throughout this work, Ω will refer to the entire image domain, while D will refer to the inpainting region.)

This analogy also shows why diffusion is required in the original inpainting problem. The natural boundary conditions for inpainting are to match the image intensity on the boundary of the inpainting region and also the direction of the isophote lines ($\vec{\tau}_I$) which for the fluid problem is effectively a generalized 'no-slip' boundary condition that requires a Navier-Stokes formulation, introducing a diffusion term. In practice nonlinear diffusion (as in Perona-Malik [PM90], and Rudin, Osher, Fatemi [ROF92]) works very well to avoid blurring of edges in the inpainting.

A different approach to inpainting was proposed by Chan and Shen [CS01a]. They introduced the idea that well-known variational image denoising and segmentation models can be easily adapted to the inpainting task by a simple modification. They proposed a minimization of

$$J[u] = \int_{\Omega} |\nabla u| \; dx + \frac{\lambda}{2} \int_{\Omega \setminus D} (u - u_0)^2 \; dx, \tag{1.4}$$

where λ is a fitting constant or Lagrange multiplier. The Euler-Lagrange equation of (1.4) is then

$$\frac{\partial u}{\partial t} = \nabla \cdot \left[\frac{\nabla u}{|\nabla u|}\right] + \lambda(u - u_0)\chi_{\Omega \setminus D}. \tag{1.5}$$

By restricting the effects of the fidelity term in these models to only the complement of the inpainting region, Chan and Shen showed that very good image completions can be obtained. The principle behind their approach can be summarized as follows: Variational denoising and segmentation models all have an underlying notion of what constitutes an image. In the inpainting region, the models of Chan and Shen reconstruct the missing image features by relying on these built-in notions.

This first model introduced by Chan and Shen used the total variation based image denoising model of Rudin, Osher, and Fatemi [ROF92] for the inpainting purpose. The model can successfully propagate sharp edges into the damaged domain. However, because the regularization term in this model exacts a penalty on the length of edges, this technique cannot connect contours across very large distances. Another caveat to the method is that it does not always keep the direction of isophotes continuous across the boundary of the inpainting domain.

Subsequently, Kang, Chan, and Shen [CSK02] introduced a new variational image inpainting model that addressed the shortcomings of the the total variation based one. The model is motivated by the work of Nitzberg, Mumford, and Shiota [NMS93], and includes a new regularization term that penalizes not merely the length of edges in an image, but the integral of the square of curvature along the edge contours. The energy is given by

$$J[u] = \int_D \phi(\kappa)|\nabla u| \; dx, \quad \kappa = \nabla \cdot \left[\frac{\nabla u}{|\nabla u|}\right], \tag{1.6}$$

with the resulting Euler-Lagrange equation

$$\frac{\partial u}{\partial t} = \nabla \cdot \Big(\phi(\kappa)\frac{\nabla u}{|\nabla u|} - \frac{\vec{t}}{|\nabla u|}\frac{\partial(\phi'(\kappa)|\nabla u|)}{\partial \vec{t}} \Big), \tag{1.7}$$

where $\frac{\partial}{\partial \vec{t}}$ is directional derivative in the direction of the tangent (isophote) vector $\vec{t} = \frac{\nabla^{\perp} u}{|\nabla u|}$. This allows both for isophotes to be connected across large distances, and their directions to be kept continuous across the edge of the inpainting region.

Following in the footsteps of Chan and Shen, Esedoglu and Shen [ES02] adapted the Mumford-Shah image segmentation model to the inpainting problem. They utilized Ambrosio and Tortorelli's elliptic approximations [AT90] to the Mumford-Shah functional. Gradient descent for these approximations leads to parabolic equations with a small parameter ε in them; they represent edges in the image by transition regions of thickness ε. These equations have the benefit that the highest order derivatives are linear. They can therefore be solved rather quickly. However, like the total variation image denoising model, the Mumford-Shah segmentation model penalizes length of edge contours, and therefore does not allow for the connection of isophotes across large distances in inpainting applications.

In order to improve the utility of the Mumford-Shah model in inpainting, Esedoglu and Shen introduced the Mumford-Shah-Euler image model that, just like the previous work [CSK02] of Kang, Chan, Shen, penalizes square of the curvature along an edge contour. Following previous work by March [MD97], they then used a conjecture of De Giorgi [Gio91] to approximate the resulting variational problem by elliptic ones. Resulting gradient descent equations are fourth order, nonlinear parabolic PDEs with a small parameter in them, and have a striking resemblance to the Cahn-Hilliard equation.

We recall very briefly the two models introduced in [ES02], and their approximations by elliptic functionals. The first one is a very simple modification of the Mumford-Shah segmentation model, and has the following form: For a given image $f(x)$, solve the minimization problem

$$\inf_{\substack{u(x)\in L^2(\Omega)\\ K\subset\Omega}} \int_{\Omega\setminus K} |\nabla u|^2\,dx + \alpha\mathrm{Length}(K) + \lambda\int_{\Omega\setminus D} (f-u)^2\,dx. \tag{1.8}$$

Here, the unknown set K is supposed to be a union of curves and approximate the edges of the given image $f(x)$. The function $u(x)$, which is also an unknown of the problem, is required to be smooth away from the edge set K by the Dirichlet energy that appears in the energy. $D \subset \Omega$ is the user supplied inpainting region. The last integral in (1.8) represents the *fidelity term*, and forces the piecewise smooth function $u(x)$ to remain close in the L^2 sense to the given image $f(x)$. The only difference of (1.8) from the original Mumford-Shah functional is that the fidelity term is integrated over $\Omega \setminus D$ instead of the entire domain Ω.

Energies of the form (1.8) are difficult to handle because part of the minimization is to be carried out over collections of curves in the plane. Ambrosio and Tortorelli [AT90] introduced elliptic energies that approximate the Mumford-Shah functional in the sense of Gamma convergence, whose numerical treatments are consequently much easier. Their approximation, when written for (1.8), takes the form:

$$MS_\varepsilon(u,z) = \int_\Omega z^2|\nabla u|^2 + \varepsilon|\nabla z|^2 + \frac{(1-z)^2}{4\varepsilon}\,dx + \lambda\int_{\Omega\setminus D}(f-u)^2\,dx. \tag{1.9}$$

Here, the function z is introduced to keep track of the edge set. As the small parameter $\varepsilon \to 0$, these energies have been rigorously proved to converge to (1.8) in the sense of Gamma convergence. The implication is that any accumulation point of minimizers of (1.9) has to be a minimizer of (1.8). These approximations are often called 'diffuse interface' approximations because for a fixed value of ε, the minimizer approximates the sharp interface problem by one in which there is an interface of thickness of order ε. Diffuse interface methods are particularly useful for problems in which topology transitions of the interface are of interest.

Esedoḡlu and Shen [ES02] introduce a variant of energy (1.8) that incorporates curvature of edge contours into the functional. It has the form:

$$MSE(u,K) = \int_{\Omega\setminus K} |\nabla u|^2 \, dx + \int_K \alpha + \beta\kappa^2 \, d\sigma + \lambda \int_{\Omega\setminus D} (u-f)^2 \, dx. \qquad (1.10)$$

where κ is the curvature of K. Based on a conjecture of E. De Giorgi [Gio91], and following previous work by March in [DVM02], they consider the following diffuse interface approximation of (1.10):

$$\begin{aligned} MSE_\varepsilon(u,z) = \int_\Omega z^2|\nabla u|^2 + \alpha\left(\varepsilon|\nabla z|^2 + \frac{1}{\varepsilon}W(z)\right) \\ + \frac{\beta}{\varepsilon}\left(2\varepsilon\Delta z - \frac{1}{\varepsilon}W'(z)\right)^2 dx + \lambda\int_{\Omega\setminus D}(u-f)^2\, dx. \quad (1.11) \end{aligned}$$

Gradient descent for (1.11) with respect to the L^2 inner product is given by the following system of coupled diffusion equations:

$$u_t = \nabla \cdot \left(z^2 \nabla u\right) + \lambda(f-u), \qquad (1.12)$$

and

$$z_t = \left(\alpha + \frac{\beta}{2\varepsilon^2}W''(z) - 4\beta\Delta\right)\left(2\varepsilon\Delta z - \frac{1}{4\varepsilon}W'(z)\right) - |\nabla u|^2 z. \qquad (1.13)$$

Finally, a different approach to the grayscale inpainting problem has been tried by Harald Grossauer and Otmar Scherzer [GS03]. In their work on image inpainting using the Ginzburg-Landau equation, they proposed treating the image data as *complex*, where the real part was the actual grayscale value of the image point, while the imaginary part was constrained to place the boundary of a circle of radius 1 in the complex plane (see the figure below).

The Ginzburg-Landau energy is

$$F(u, \nabla u) = \frac{1}{2} \int_\Omega | - i\nabla u|^2 + \alpha |u|^2 + \frac{\beta}{2} |u|^4 \, dx, \tag{1.14}$$

where α and β are constants ($\alpha < 0$, $\beta > 0$), and $u(x,t)$ is again the phase of a point of the material under study. The steepest descent method then provides the Ginzburg-Landau equation,

$$\frac{\partial u}{\partial t} = \Delta u + \frac{1}{\varepsilon^2}(1 - |u|^2)u. \tag{1.15}$$

The substitution $u(x,t) = u_1(x,t) + iu_2(x,t)$ is inserted into equation (1.15), with the initial values of $u_2(x,t)$ set to

$$u_2(x,0) = \sqrt{1 - u_1(x,0)^2}. \tag{1.16}$$

This leads to a coupled system of equations for $u_1(x,t)$ and $u_2(x,t)$, which Grossauer and Scherzer solved by an explicit numerical scheme assuming the Dirichlet boundary conditions $u(x,t)|_{\partial\Omega} = u(x,0)|_{\partial\Omega}$ (see [GS03]).

In this paper, we consider a simple model that still has many of the desirable properties of the model introduced in [ES02], but for which there are very fast computational techniques available. In particular, we show that in the case of binary images, a slightly modified Cahn-Hilliard equation allows us to get inpaintings as good as the ones in previous papers, but much more quickly (see also [BEGar]).

The Cahn-Hilliard equation has some features that make it inherently appealing for inpainting purposes. The ability to impose boundary conditions for both the solution $u(x)$ and its derivative ∇u is one of the great advantages of fourth order models. Indeed, this allows image information generated by the model in the inpainting region D to match the original image data defined on $\Omega \setminus D$ not

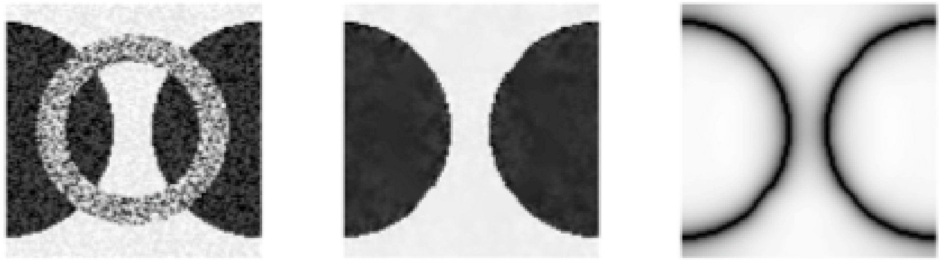

Figure 1.1: Image from [She03]. Inpainting problem solved by using the Mumford-Shah inpainting technique, shown as an example. Note that the isophotes are not smoothly continued at the boundary of the inpainting region.

only in intensity, but also in isophote directions. That means our model should edges into the inpainting domain without introducing kinks at the boundary ∂D.

In figure 1.2 one can see how isophotes are not cleanly continued by the Mumford-Shah inpainting model, which is a second order inpainting method (see [She03] for more detail on the Mumford-Shah model). A fourth order inpainting model based on the Cahn-Hilliard equation will address this isophote continuation problem. Chapters 2 and 4 go into detail on this topic.

Another feature of an inpainting model based on the Cahn-Hilliard equation, that will be shown in chapter 4, is the potential to inpaint across large gaps. Below is a figure which shows how a street scene obscured by text can be inpainted using the method described in [BSC00]. Notice that the vertical poles directly in back of the horse's head in the image are not connected. This is a long-range inpainting connection problem; an example of this will be shown in chapter 4.

1.4 Origins of the Cahn-Hilliard equation

When a mixture of two metallic components is heated, and then rapidly cooled to a lower temperature, a sudden phase separation can occur. This separation

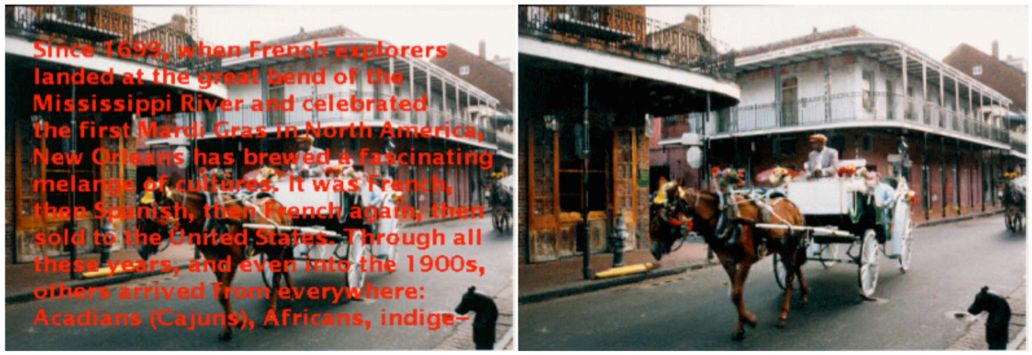

Figure 1.2: Image from [BSC00]. Inpainting problem solved by using the method described in [BSC00] by Bertalmio et. al.

of the metal alloy (for example, Au-Ni alloys) into two components, via cooling, is called *spinodal decomposition*. Understanding the process of this segregation, as well as finding any steady states that may remain after cooling has been the subject of much research in the 20th century.

John Cahn and John Hilliard began work on the spinodal decomposition problem in the late 1950s (see [CH58]). They proposed a chemical model that has the following energy:

$$F(c) \;=\; \int \Big(f(c) + \kappa(\nabla c)^2 \Big)\, dV, \tag{1.17}$$

where $f(c)$ is the free-energy density of the material $c(x, y, z, t)$, and $\kappa(\nabla c)^2$ is the additional free-energy density if the material is in a gradient in composition (i.e., in a transition between two states c_A and c_B). Additionally, mass is assumed to be conserved in this system, giving

$$\int c\; dV = C \tag{1.18}$$

with C being a constant. The boundary conditions are chosen to prohibit the flow of material into or out of the confined volume,

$$\partial_\nu c = \partial_\nu \Big(f(c) + \kappa(\nabla c)^2 \Big) = 0 \text{ on } dV, \tag{1.19}$$

but since $\partial_\nu f(c) = f'(c)\partial_\nu c$, we have the simplified boundary conditions

$$\partial_\nu c = \partial_\nu \Delta u = 0 \text{ on } dV. \tag{1.20}$$

Here, ∂_ν is taken to mean the directional derivative of c normal to the boundary dV.

The Cahn-Hilliard equation is then derived in the following manner. First,

$$\mu_A - \mu_B = \nabla F(c) = \frac{\partial f}{\partial c} - 2\kappa\Delta c, \tag{1.21}$$

where $\mu_A - \mu_B$ is the chemical potential difference between the phase states A and B, and $\nabla F(c)$ is the variational derivative of the energy $F(c)$.

Next, the following relation is used:

$$J_B = -J_A = M\nabla(\mu_A - \mu_B), \tag{1.22}$$

where J_A, J_B refer to the diffusional flux from the states A and B, respectively, and M is a constant that represents mobility. Finally, the time rate of change of the concentration $c(x, y, z, t)$ is equal to the divergence of the flux $J_B = -J_A$,

$$\nabla \cdot J_B = \frac{\partial c}{\partial t}. \tag{1.23}$$

Combining equations (1.21), (1.22), and (1.23), one has the well-known Cahn-Hilliard equation (see [Hil70] for additional details):

$$\frac{\partial c}{\partial t} = M\Delta(\frac{\partial f}{\partial c} - 2\kappa\Delta c). \tag{1.24}$$

The Cahn-Hilliard equation can also be derived as a gradient flow from an energy, as has been shown by Fife [Fif00]. Assume the spinodal decomposition of a two-phase system will minimize the following energy:

$$E(u) = \int_\Omega \Big(\frac{\varepsilon^2}{2}|\nabla u(x)|^2 + W(u)\Big)\, dx, \tag{1.25}$$

where $W(u)$ again is a double-welled potential energy having two minima that represent the two phases. The $\frac{\varepsilon^2}{2}|\nabla u(x)|^2$ term is added to the energy integral to allow smooth transitions between the two stable states. In reference to the original Cahn-Hilliard equation (1.24), notice that $f(c)$ is replaced with $W(u)$ for equation (1.25). Also, M and κ from equation (1.24) are mapped into the parameter ε in equation (1.25).

Also note that the integral is assumed (for our purposes) to be taken over a domain $\Omega \in R^2$. The boundary conditions mirror our previous discussion:

$$\partial_\nu u = \partial_\nu \Delta u = 0. \tag{1.26}$$

This formulation is turned into a gradient flow by equating

$$\langle \frac{\partial u}{\partial t}, v \rangle_H \;=\; -\langle \nabla E(u), v \rangle_H \tag{1.27}$$

where $\nabla E(u)$ represents the variational derivative of the energy $E(u)$ with respect to a particular Hilbert space H of functions,

$$\langle \nabla E(u), v \rangle_H \;=\; \frac{\partial}{\partial t} E(u + tv)|_{t=0}. \tag{1.28}$$

When $v \in L^2(\Omega)$ or $v \in H^k(\Omega)$ $(k > 0)$ are used as the Hilbert spaces, one arrives at nonlocal evolution laws for $u(x,t)$. These have been rejected by researchers on the argument that the physics dictates that the evolution of $u(x,t)$ should proceed from local interactions. For an extensive discussion of this, see [Fif00].

However, when the zero-average subspace of the dual of H^1 is used, known as H^{-1}, the result of the gradient flow is the Cahn-Hilliard equation. In this space we have that, for $v \in H^{-1}$,

$$\int_\Omega v \; dx = 0, \tag{1.29}$$

which occurs if and only if, for $v = \Delta\Phi$,

$$\int_\Omega \Phi \ dx = 0. \tag{1.30}$$

The scalar product of H^{-1} is then defined as

$$\langle v_1, v_2 \rangle_{H^{-1}} = \langle \nabla\Phi_1, \nabla\Phi_2 \rangle_{L^2}, \tag{1.31}$$

where $v_1 = \Delta\Phi_1$ and $v_2 = \Delta\Phi_2$.

Applying this to equation (1.28),

$$\frac{\partial}{\partial t} E(u + t\Delta\Phi)|_{t=0} \ = \ \int_\Omega \Big(W'(u) - \varepsilon^2 \Delta u \Big) \Delta\Phi \ dx, \tag{1.32}$$

which after integration by parts leads to

$$\int_\Omega -\nabla[W'(u) - \varepsilon^2 \Delta u] \nabla\Phi \ dx, \tag{1.33}$$

which is now in the form of (1.31). Using equation (1.31) with the term $-\nabla[W'(u) - \varepsilon^2 \Delta u]$ assuming the role of $\nabla\Phi_1$,

$$\langle -\nabla[W'(u) - \varepsilon^2 \Delta u], \nabla\Phi \rangle_{L^2} = \langle -\Delta[W'(u) - \varepsilon^2 \Delta u], v \rangle_{H^{-1}}. \tag{1.34}$$

Within the construct of the gradient flow equation (1.27), we finally arrive at

$$\frac{\partial u}{\partial t} = \Delta[W'(u) - \varepsilon^2 \Delta u]. \tag{1.35}$$

By making the substitution $t \to \varepsilon t$, we obtain the form used throughout the later chapters of this paper,

$$\frac{\partial u}{\partial t} = -\Delta[\varepsilon \Delta u - \frac{1}{\varepsilon} W'(u)]. \tag{1.36}$$

1.5 Solutions of the Cahn-Hilliard equation

Due to the bi-stable potential $W(u)$ in the Cahn-Hilliard energy (1.36), solutions exhibit a segregation of species. From the gradient term in the energy, a diffuse interface between the separated states forms. This interface is of $O(\varepsilon)$ in size, and upon taking $\varepsilon \to 0$ in equation (1.36), one recovers Mullins-Sekerka interface dynamics (see [MS63]). Pego in 1989 [Peg89] used matched asymptotics to solve for the interface. Later, Alikakos, Bates, and Chen in 1994 proved Pego's interface solution rigorously [ABC94].

In our work, $W(u)$ in equation (1.36) is taken to be the polynomial $W(u) = u^2(u-1)^2$, and so $W'(u) = 4u^3 - 6u^2 + 2u$. Thus $W'(u)$ has 3 zeros, all of which constitute solutions to the Cahn-Hilliard equation (1.36).

Interestingly, an exact solution (albeit not very exciting) exists. A family of steady-state solutions can be found of the form

$$u(x) \;=\; a\tanh\left(\frac{\pm ax}{\varepsilon} + b\right) \;+\; c \tag{1.37}$$

where a, b, and c are constants that depend on the precise form of $W'(u)$. This solution consists of two uniform regions, separated by a diffuse interface.

However, the solution of interest for inpainting purposes will often be some form of *three* uniform regions separated by *two* diffuse interfaces. The long term stability of such solutions is unknown. However we will approach the issues of existence and uniqueness of such a proposed solution in chapter 2.

The stability of a solution to (1.36) is very much related to the diffuse interface mobility. In this aspect the Cahn-Hilliard equation shares properties of the Hele-Shaw model, where the transport of mass across very finely connected regions has been observed [Gla03] to occur on very slow time scales. It is therefore difficult to say that a particular solution of the Cahn-Hilliard equation is stable for all time. We will investigate the issue of stability in more detail in chapters 2 and 4. The work presented in chapters 4 and 5 shows my empirical investigations of the modified Cahn-Hilliard equation, of course done under the guidance of Dr. Bertozzi.

As a final comment, I would like to make clear the roles and responsibilites for the research presented in this thesis. I personally was responsible for the numerical simulations and programming, including parameter estimations. I contributed some parts to the analysis portions presented in chapter 2, but that portion was for the most part a collaborative effort where Dr. Andrea Bertozzi and Dr. Selim Esedoglu played major roles in developing the analytical foundations. The numerical schemes explained in chapter 3 were originally developed by Dr. Bertozzi while she was at Duke University, and later utilized in an early test problem with the collaboration of Dr. Esedoglu. I have considerably expanded the exposition of the numerical scheme in chapter 3.

CHAPTER 2

Analysis

2.1 Proposed model

This chapter cites numerous results from [BEG06]. We consider a binary image (i.e shape) inpainting model that is a much simplified version of the Esedoḡlu-Shen model from the chapter 1. The key observation is that the fourth order gradient flow in the Esedoḡlu-Shen model has features in common with the Cahn-Hilliard equation, which is a much simpler model for which fast solution techniques are available [BEGar, VR03]. It is therefore natural to ask if a simpler model can be used directly for inpainting.

Let $f(x)$ be a given binary image, and suppose that $D \subset \Omega$ is the inpainting domain. We propose solving the following equation to steady state in order to construct an inpainted version $u(x)$ of $f(x)$:

$$u_t = -\Delta \left(\varepsilon \Delta u - \frac{1}{\varepsilon} W'(u) \right) + \lambda(x)(f - u). \tag{2.1}$$

where

$$\lambda(x) = \begin{cases} 0 & \text{if } x \in D, \\ \lambda_0 & \text{if } x \in \Omega \setminus D \end{cases}$$

$u(x,t)$ satisfies $\frac{\partial u}{\partial \nu} = \frac{\partial \Delta u}{\partial \nu} = 0$ on $\partial\Omega$, and again $W(u) = u^2(u-1)^2$.

Equation (2.1) is identical to the standard Cahn-Hilliard equation [BF93, NS84] except for the second term on the right hand side. This term is there to keep the solution constructed close to the given image $f(x)$ in the complement of the inpainting domain, where there is image information available. We mention here that such phase field models have been used for other applications such as shape recovery in computer vision [DVM02].

Equation (2.1) is not derived as a gradient flow for an energy; however, it can be thought of as a superposition of gradient descents for two different energies. Indeed, the Cahn-Hilliard equation is the gradient flow with respect to the H^{-1} inner product [TC94] of the following energy, which was discussed in chapter 1:

$$E_\varepsilon(u) := \int_\Omega \left(\frac{\varepsilon}{2}|\nabla u|^2 + \frac{1}{\varepsilon}W(u)\right) dx. \tag{2.2}$$

This is the energy of Modica-Mortola [MM77], which has been rigorously shown to approximate the perimeter of sets in the sense of Gamma convergence:

$$E_\varepsilon \xrightarrow{\Gamma} E(u) := \begin{cases} \mathrm{Per}(\Sigma) & \text{if } u(x) = \mathbf{1}_\Sigma(x) \text{ for some } \Sigma \subset \Omega, \\ +\infty & \text{otherwise.} \end{cases}$$

When $\lambda(x) \equiv 0$, equation (2.1) thus decreases (2.2); it can also be easily seen that in this case the solution preserves total image intensity (i.e. $\int_\Omega u(x,t)\,dx$ is constant in t). The dynamics of (2.1) in this case has been studied extensively. For instance, it is well-known that under (2.1) with $\lambda(x) \equiv 0$, arbitrary initial data form interfaces of thickness approximately ε at a fast time scale; these interfaces separate regions where the solution is approximately either 0 or 1 (location of wells for the potential W). The fact that energy (2.2) is decreased suggests that the subsequent evolution involves some sort of coarsening of this configuration of regions. Indeed, as $\varepsilon \to 0$, at a slower time scale the interfaces approximate the solution of the Mullins-Sekerka problem [ABC94, Peg89].

When $\lambda(x) \not\equiv 0$, equation (2.1) is no longer a gradient descent for (2.2); the second term in the right hand side of (2.1) is gradient descent with respect to the

L^2 inner product for the pointwise energy:

$$\frac{\lambda}{2}\int_{\Omega}(u-f)^2\,dx. \tag{2.3}$$

Our proposed model (2.1) can thus be thought of as a superposition of gradient descent with respect to H^{-1} inner product for (2.2), and gradient descent with respect to L^2 inner-product for (2.3). However, it is *not* the gradient descent, either in H^{-1} or L^2 inner product, for the sum of the energies (2.2) and (2.3).

An important distinction of model (2.1) from those of Bertalmio et. al. is that no explicit boundary conditions are imposed at the boundary ∂D of the inpainting region D. However, we will show in Section 2.3 that in the limit that $\lambda_0 \to \infty$, stationary solutions of (2.1) converge to the solution of the following equation:

$$\begin{aligned} &-\Delta\left(\varepsilon\Delta u - \frac{1}{\varepsilon}W'(u)\right) = 0 \text{ in } x \in D,\\ &u(x) = f(x) \text{ on } x \in \partial D, \text{ and}\\ &\nabla u = \nabla f \text{ on } x \in \partial D. \end{aligned} \tag{2.4}$$

This is proved under the condition that the given function $f(x) \in C^2(\Omega)$. The fact that (2.1) is fourth order naturally leads to the two boundary conditions (2.4) in the limit of large λ. We note that this feature is not special to the particular nonlinear equation considered here, but is due to the highest order term on the right hand side of (2.1). The rigorous results of sections 2.3 and 2.4 require only the highest order term to complete the analysis. The rest of the work in those sections is to show that the lower order terms, which are responsible for the phase separation, do not adversely affect the results. We therefore expect that solving equation (2.1) with a very large choice of the constant λ_0 will approximate a solution of (2.4).

After addressing the case $\lambda \to \infty$ for $f \in C^2$, where we take ε first to be one, we then consider f a smooth approximation of a binary function, where the smoothing is on a scale ε, the diffuse interface scale. We show that the same estimates hold as in the completely smooth case, except that now λ depends on ε. In practice, we do not find any significant numerical hardship regarding the large value of λ when ε is small.

2.2 Global existence of weak solutions of the modified Cahn-Hilliard equation

Before discussing the steady state problem, we show that well-posedness of the dynamic problem follows from classical methods for the case $\lambda_0 = 0$.

Consider the time dependent problem on a compact region $\Omega \subset \mathbb{R}^2$ with an inpainting region $D \subset \Omega$,

$$u_t = -\Delta(\varepsilon\Delta u - \frac{1}{\varepsilon}W'(u)) + \lambda_0(f \ - \ u)\chi_{\Omega\setminus D}. \tag{2.5}$$

Following III, 4.2 in [Tem97] for the case $\lambda_0 = 0$, we define $V = \{\phi \in H^2(\Omega) \mid \frac{\partial\phi}{\partial\nu} = 0 \quad \text{on} \quad \partial\Omega\}$. We define a weak solution of the evolution equation (2.5) as one that satisfies

$$\frac{d}{dt}\langle u, v\rangle + \langle \varepsilon\Delta u, \Delta v\rangle - \langle\frac{1}{\varepsilon}W'(u), \Delta v\rangle = \langle\lambda(x)(f-u), v\rangle, \quad \forall v \in V, \tag{2.6}$$

where $\langle ., .\rangle$ specifies the L^2 inner product.

We establish the following global existence and uniqueness theorem.

Theorem 1. *For every u_0 in $L^2(\Omega)$, and every $T > 0$, the initial-boundary value problem (2.6) has a unique solution u which belongs to $C([0,T]; L^2(\Omega)) \cap L^2(0,T;V)$.*

The proof of existence follows a similar argument as in [Tem97] for $\lambda = 0$. We require an L^2 estimate that includes the additional fidelity term. In fact we show that this gives a global in time bound for u in L^2 when λ is sufficiently large.

Lemma 2. *Given a weak solution as described above, there exist constants* $C(\varepsilon, \lambda, f) > 0$ *and* $\theta(\lambda, f, \varepsilon)$ *so that*

$$\frac{1}{2}\frac{d}{dt}\int_\Omega u^2\,dx \le C(\varepsilon,\lambda,f) - \theta\int_{\Omega/D} u^2\,dx, \tag{2.7}$$

for all $t \ge 0$. *For* λ *sufficiently large,* $\theta > 0$.

This lemma establishes an a priori bound for the L^2 norm of the solution u; this bound is *uniform* in time for λ sufficiently large. We expect that it would therefore play an important role in, for example, establishing existence of steady states for the modified Cahn-Hilliard equation considered in this paper.

Proof: We first reference a standard interpolation inequality:

$$\int_\Omega |\nabla u|^2\,dx \le \delta\int_\Omega (\Delta u)^2\,dx + \frac{C}{\delta}\int_\Omega u^2\,dx \tag{2.8}$$

By the L^1 version of Poincare's inequality, together with the observation that the domain of integration in the second integral of equation (2.8) can be taken to be something smaller than Ω (at the expense of larger constants, but no matter):

$$\int_\Omega u^2\,dx \le C\int_\Omega |\nabla(u^2)|\,dx + C\int_{\Omega\setminus D} u^2\,dx, \tag{2.9}$$

where C depends on the size of D compared to Ω. By Hölder's inequality we also have that (for some α small enough):

$$\int_\Omega |\nabla(u^2)|\,dx \le |\Omega|^{\frac{1}{2}}\left(\int_\Omega u^2|\nabla u|^2\,dx\right)^{\frac{1}{2}} \le \frac{\alpha}{2}\int_\Omega u^2|\nabla u|^2\,dx + \frac{C}{2\alpha} \tag{2.10}$$

Putting the last three inequalities together:

$$\int_\Omega |\nabla u|^2\,dx \le \delta\int_\Omega(\Delta u)^2\,dx + \frac{C\alpha}{2\delta}\int_\Omega u^2|\nabla u|^2\,dx + \frac{C}{\delta}\int_{\Omega\setminus D} u^2\,dx + \frac{C}{2\alpha\delta} \tag{2.11}$$

Now computing the rate of change of the L^2 norm of the solution, we get that:

$$\begin{aligned}\frac{1}{2}\frac{d}{dt}\int_\Omega u^2\,dx &= -\varepsilon\int_\Omega (\Delta u)^2\,dx + \frac{1}{\varepsilon}\int_\Omega u\Delta W'(u)\,dx + \lambda\int_{\Omega\setminus D} u(f-u)\,dx \\ &= -\varepsilon\int_\Omega (\Delta u)^2\,dx - \frac{1}{\varepsilon}\int_\Omega W''(u)|\nabla u|^2\,dx + \lambda\int_{\Omega\setminus D} u(f-u)\,dx\end{aligned} \tag{2.12}$$

where we integrated by parts on the second term in the right hand side.

Using the fact that $W''(\xi) \geq \gamma\xi^2 - C$ for all ξ, for some constants γ and C, in (2.12):

$$\frac{1}{2}\frac{d}{dt}\int_\Omega u^2\,dx \leq -\varepsilon\int_\Omega (\Delta u)^2 dx - \frac{\gamma}{\varepsilon}\int_\Omega u^2|\nabla u|^2\,dx + \frac{C}{\varepsilon}\int_\Omega |\nabla u|^2 + \lambda\int_{\Omega\setminus D} u(f-u)\,dx \tag{2.13}$$

We now put everything together as follows: First, writing the last term above as

$$\lambda\int_{\Omega/D} uf dx - \lambda\int_{\Omega/D} u^2 dx \leq \frac{\lambda}{2}\int_{\Omega/D} f^2 dx - \frac{\lambda}{2}\int_{\Omega/D} u^2 dx,$$

we use inequality (2.9) in order to bound the last term of the inequality above as follows:

$$\begin{aligned}\frac{1}{2}\frac{d}{dt}\int_\Omega u^2\,dx \leq -\varepsilon\int_\Omega (\Delta u)^2\,dx - \frac{\gamma}{\varepsilon}\int_\Omega u^2|\nabla u|^2\,dx + \frac{C}{\varepsilon}\int_\Omega |\nabla u|^2\,dx \\ + \frac{\lambda}{2}\int_{\Omega\setminus D} f^2\,dx + \frac{\lambda}{2}\int_\Omega |\nabla(u^2)|\,dx - \frac{\lambda}{2C}\int_\Omega u^2\,dx.\end{aligned}$$

Now use inequality (2.10) with $\alpha = \delta_1$ to estimate the next to last term in the inequality above:

$$\begin{aligned}\frac{1}{2}\frac{d}{dt}\int_\Omega u^2\,dx \leq -\varepsilon\int_\Omega (\Delta u)^2 dx - \frac{\gamma}{\varepsilon}\int_\Omega u^2|\nabla u|^2\,dx + \frac{C}{\varepsilon}\int_\Omega |\nabla u|^2\,dx + \frac{\lambda}{2}\int_{\Omega\setminus D} f^2\,dx \\ + \frac{\lambda\delta_1}{4}\int_\Omega u^2|\nabla u|^2\,dx + \frac{C\lambda}{4\delta_1} - \frac{\lambda}{2C}\int_\Omega u^2\,dx\end{aligned}$$

Now use inequality (2.11) with $\alpha = \delta_1$ and $\delta = \delta_2$ to estimate the $\int |\nabla u|^2\,dx$ term in the inequality above as follows:

$$\begin{aligned}\frac{1}{2}\frac{d}{dt}\int_\Omega u^2\,dx \le &-\varepsilon\int_\Omega(\Delta u)^2\,dx-\frac{\gamma}{\varepsilon}\int_\Omega u^2|\nabla u|^2\,dx+\frac{C\delta_2}{\varepsilon}\int_\Omega(\Delta u)^2\,dx+\frac{C\delta_1}{2\varepsilon\delta_2}\int_\Omega u^2|\nabla u|^2\,dx\\ &+\frac{C}{2\varepsilon\delta_1\delta_2}+\frac{C}{\varepsilon\delta_2}\int_{\Omega\setminus D}u^2\,dx+\frac{\lambda}{2}\int_{\Omega\setminus D}f^2\,dx+\frac{\lambda\delta_1}{4}\int_\Omega u^2|\nabla u|^2\,dx\\ &+\frac{C\lambda}{4\delta_1}-\frac{\lambda}{2C}\int_\Omega u^2\,dx.\end{aligned}$$

We now try to satisfy the following conditions with our choice of the constants $\delta_1, \delta_2, \alpha$, and λ:

1. $\frac{C\delta_2}{\varepsilon} < \varepsilon$, i.e. $\delta_2 < \frac{\varepsilon^2}{C}$,
2. $\frac{C\delta_1}{2\varepsilon\delta_2} + \frac{\lambda\delta_1}{4} < \frac{\gamma}{\varepsilon}$,
3. $\frac{C}{\varepsilon\delta_2} < \frac{\lambda}{2C}$,

To satisfy the first condition, take $\delta_2 = \frac{1}{8C}\varepsilon^2$. Then, to satisfy the third, we can choose any $\lambda \ge \frac{16C^3}{\varepsilon^3}$. To satisfy the second, choose $\delta_1 < \frac{4\varepsilon^2\gamma}{16C^2+\lambda\varepsilon^3}$. With these choices, we end up with the following inequality:

$$\frac{1}{2}\frac{d}{dt}\int_\Omega u^2\,dx \le C(\varepsilon,\lambda,f) - \theta\int_\Omega u^2\,dx$$

where $\theta > 0$. For any λ, Grönwall's lemma implies an a priori bound on the L^2 norm of u on any finite time interval $[0,T)$. Moreover, for sufficiently large λ, we obtain a uniform in time bound on the L^2 norm of $u(\cdot,t)$:

$$\exists M > 0 \text{ such that } \|u(\cdot,t)\|_{L^2} \le M \text{ for all } t \ge 0. \quad \square$$

Remark: In the above analysis, the λ needed to obtain a negative θ depends on ϵ and the size of the inpainting region compared to Ω.

Following the remaining arguments in [Tem97] one can establish global existence and uniqueness of a weak solution to the modified Cahn-Hilliard equation.

We are not aware of any Lyapunov function for this problem, as in the original CH model. However, we observe in our numerical simulations that the solution quickly approaches a steady state as t increases; as we mentioned before, the existence of such are strongly suggested by the estimate given above. Moreover, the steady state solution appears to inherit the regularity of the original parabolic problem. In the next section we show that existence of an H^2 solution of the steady state problem guarantees that the intended boundary conditions for the inpainting problem are satisfied as $\lambda \to \infty$. In the analysis, λ depends on ϵ, however this dependence is not something that, in practice, causes us hardship in the computation. We prove this result while noting that convergence of the time dependent solution to the steady state problem remains unaddressed.

2.3 Fidelity and boundary conditions

The fidelity parameter λ in (2.1) enforces the original image outside of the inpainting region. One might expect that as λ gets large, the existing region enforces some kind of effective boundary conditions on the inpainting region. In this section we prove this rigorously for the steady state problem. As we mentioned earlier, these solutions turn out to approximate a solution of (2.4). Our results establish rigorously a connection between the inpainting technique used by Bertalmio et. al. (who prefer to impose boundary conditions at the edge of the inpainting domain D) and that of Chan et. al. (who prefer to use a *fidelity term*, similar to the second term in the right hand side of our model (2.1)). In this section we consider the case $\varepsilon = 1$, and smooth (grayscale) f. In the next section we show how to extend these results to binary f and small ε.

2.3.1 Key estimates

We require the following version of the Poincaré inequality.

Lemma 3. *(Poincaré inequality) Let $\Omega \subset \mathbb{R}^N$ be a bounded domain with Lipschitz boundary. There exists a constant $C = C(\Omega) > 0$ such that if $v(x) \in C^1(\Omega)$ with $v = (u - \bar{u})^2$ for some $u \in C^1(\Omega)$ and $\bar{u} := \frac{1}{|\Omega|}\int_\Omega u\,dx$, then*

$$\int_\Omega v^2\,dx \leq C\int_\Omega |\nabla v|^2\,dx.$$

Proof: Suppose not. Then there exists a sequence $\{u_j\}_{j=1}^\infty \subset C^1(\Omega)$ such that

$$\int_\Omega v_j^2\,dx > j\int_\Omega |\nabla v_j|^2\,dx$$

where $v_j = (u_j - \bar{u}_j)^2$ for some $u_j \in C^1(\Omega)$, and $v_j \neq 0$. By normalizing, we make sure that

$$\int_\Omega v_j^2\,dx = 1 \text{ and } \bar{u}_j := \frac{1}{|\Omega|}\int_\Omega u_j\,dx = 0 \text{ for all } j.$$

Then, the functions v_j are bounded uniformly in $L^2(\Omega)$ and

$$\int_\Omega |\nabla v_j|^2\,dx < \frac{1}{j}.$$

By Rellich's theorem, by passing to a subsequence if necessary, we may assume that v_j converge to some v_∞ in the $L^2(\Omega)$ sense and pointwise a.e.

Let $w_j(x) := \max^2\{0, u_j(x)\}$. Then:

$$\begin{aligned}\int_\Omega |\nabla w_j|^2\,dx &\leq \int_\Omega 4\Big(\max\{0, u_j(x)\}\Big)^2|\nabla u_j|^2\,dx \leq \int_\Omega 4u_j^2|\nabla u_j|^2\,dx \\ &= 4\int_\Omega |\nabla v_j|^2\,dx \longrightarrow 0 \text{ as } j \to \infty.\end{aligned}$$

Once again by Rellich, we may assume that the sequence w_j converges to some w_∞ in $L^2(\Omega)$. By lower semicontinuity,

$$\int_\Omega |\nabla w_\infty|^2\,dx \leq \liminf_{j\to\infty}\int_\Omega |\nabla w_j|^2\,dx = 0.$$

That means w_∞ is a constant.

The very same argument applied to $\tilde{w}_j(x) := \min^2\{0, u_j(x)\}$ shows that up to passing to subsequences, we may assume that $\tilde{w}_j \to \tilde{w}_\infty$ in $L^2(\Omega)$ and pointwise a.e., where $\tilde{w}_\infty$ is a constant.

Thus, for a.e. $x \in \Omega$, we have that $\sqrt{w_j(x)} = \max\{0, u_j(x)\}$ converges to $\sqrt{w_\infty}$ and $\sqrt{\tilde{w}_j(x)} = -\min\{0, u_j(x)\}$ converges to $\sqrt{\tilde{w}_\infty}$. Since $u_j(x) = \max\{0, u_j(x)\} + \min\{0, u_j(x)\}$, we have that

$$\lim_{j\to\infty} u_j(x) = C := \sqrt{w_\infty} - \sqrt{\tilde{w}_\infty} \text{ for a.e. } x \in \Omega.$$

Moreover, since the sequence $\{av_j^2 + b\}$ dominates $\{(u_j - C)^4\}$ for some $a, b \in \mathbb{R}$, and $\{v_j\}$ converges in L^2, we get that the sequence $\{u_j\}$ converges to the constant C in $L^4(\Omega)$. But $\bar{u}_j = 0$, so in fact we must have $C = 0$. This contradicts the fact $\int u_j^4\, dx = \int v_j^2\, dx = 1$.

If necessary, we pass to a further subsequence to ensure that v_j converge to the constant $|\Omega|^{\frac{1}{2}}$ pointwise a.e. Then, by definition of v_j, we have:

$$\text{For a.e. } x \in \Omega, \text{ either } u_j(x) \to |\Omega|^{\frac{1}{4}} \text{ or } u_j(x) \to -|\Omega|^{\frac{1}{4}}.$$

But in fact, we have the following:

<u>Claim:</u> Either $u_j \to |\Omega|^{\frac{1}{4}}$ for a.e. $x \in \Omega$, or $u_j \to -|\Omega|^{\frac{1}{4}}$ for a.e. $x \in \Omega$.

Proof of Claim: Suppose not. Then there exists a subset Σ of Ω such that $|\Sigma| > 0$, $|\Omega \setminus \Sigma| > 0$, and

$$u_j(x) \to |\Omega|^{\frac{1}{4}} \text{ for a.e. } x \in \Sigma, \text{ and } u_j(x) \to -|\Omega|^{\frac{1}{4}} \text{ for a.e. } x \in \Omega \setminus \Sigma.$$

Let $\eta(x) := \max\{0, x^2\}$, and consider the sequence $w_j := \eta(u_j)$. Then $w_j \to |\Omega|^{\frac{1}{2}} \mathbf{1}_\Sigma$ in L^2, and

$$\begin{aligned}\int_\Omega |\nabla w_j|^2\, dx = \int_\Omega |\eta'(u_j)|^2 |\nabla u_j|^2\, dx \le \int_\Omega u_j^2 |\nabla u_j|^2 \\ \le \int_\Omega |\nabla v_j|^2 \to 0 \text{ as } j \to \infty.\end{aligned}$$

which is impossible, proving the claim. $\square$

Returning to the proof of the Lemma, in light of the claim above, we now assume with no loss of generality that $u_j \to |\Omega|^{\frac{1}{4}}$ for a.e. $x \in \Omega$. Since u_j are dominated by $1+v_j$, and since $1+v_j \to 1+|\Omega|^{\frac{1}{2}}$ in $L^2(\Omega)$, we get that $u_j \to |\Omega|^{\frac{1}{4}}$ in $L^2(\Omega)$. This contradicts the assumption that $\bar{u}_j = 0$ for all j, proving the lemma. $\square$

Lemma 4. *Let $\Omega \subset \mathbb{R}^N$ be a bounded domain with Lipschitz boundary. Let D be a compactly included subdomain of Ω, also with Lipschitz boundary. There exist constants C_1, C_2, and C_3 such that if $u(x) \in C^1(\Omega)$, then*

$$\begin{aligned}\int_\Omega u^4\,dx \leq & C_1 \left(\frac{1}{|\Omega \setminus D|}\int_{\Omega\setminus D} u\,dx\right)^4 + C_2 \int_\Omega u^2|\nabla u|^2\,dx \\ & + C_3 \left(\frac{1}{|\Omega \setminus D|}\int_{\Omega\setminus D} u\,dx\right)^2 \int_\Omega |\nabla u|^2\,dx.\end{aligned}$$

Proof: Define the function v to be:

$$v(x) := \left(u(x) - \frac{1}{|\Omega \setminus D|}\int_{\Omega\setminus D} u(x)\,dx\right)^2.$$

The standard Poincaré inequality implies:

$$\int_\Omega v^2\,dx \leq C \int_{\Omega\setminus D} v^2\,dx + C\int_\Omega |\nabla v|^2\,dx. \tag{2.14}$$

On the other hand, Lemma 3 implies:

$$\int_{\Omega\setminus D} v^2\,dx \leq C \int_{\Omega\setminus D} |\nabla v|^2\,dx. \tag{2.15}$$

Combining inequalities (2.14) and (2.15) we get:

$$\int_\Omega v^2\,dx \leq C \int_\Omega |\nabla v|^2\,dx.$$

Writing the last inequality in terms of u yields the conclusion of the present lemma after a few elementary manipulations. $\square$

Proposition 1. *Let u be an H^2 weak solution of the PDE*

$$-\Delta\Big(\Delta u - W'(u)\Big) + \lambda(x)(f-u) = 0,$$

that is

$$\langle \Delta u, \Delta v\rangle - \langle W'(u, \Delta v\rangle = \langle \lambda(x)(f-u), v\rangle, \quad \forall v \in V. \tag{2.16}$$

where

$$\lambda(x) = \begin{cases} 0 & \text{if } x \in D, \\ \lambda_0 & \text{if } x \in \Omega \setminus D \end{cases}$$

with $\lambda_0 \geq 0$. Assume that $f \in C^2(\Omega)$. Then there exists constants C_1 and C_2 independent of λ_0, depending only on f, so that

$$\begin{aligned} &\int_\Omega \Big(\Delta u\Big)^2 dx \leq C_1, \text{ and} \\ &\int_{\Omega\setminus D} \Big(u - f\Big)^2 dx \leq \frac{C_2}{\lambda_0}. \end{aligned} \tag{2.17}$$

Proof: First, we consider a test function $v \equiv 1$ to obtain

$$\int_{\Omega\setminus D} u\, dx = \int_{\Omega\setminus D} f\, dx. \tag{2.18}$$

where we used the fact $\lambda = 0$ in D. Then, taking a test function $v = (u - f)$, we get

$$\begin{aligned} 0 &= \int_\Omega -\Big((\Delta u - \Delta f)(\Delta u - W'(u)) + \lambda(x)(u-f)^2\Big)\, dx \\ &= -\int_\Omega \Big(\Delta u\Big)^2 dx - \int_\Omega \lambda(x)(f-u)^2\, dx + (I) + (II) \end{aligned} \tag{2.19}$$

where

$$\begin{aligned} (I) &:= \int_\Omega W'(u)\Delta u\, dx, \text{ and} \\ (II) &:= \int_\Omega \Big(\Delta u - W'(u)\Big)\Delta f\, dx. \end{aligned}$$

By first applying integration by parts we have

$$
\begin{aligned}
(I) &= -\int_\Omega W''(u)|\nabla u|^2\,dx \\
&\leq \int_\Omega -\gamma u^2|\nabla u|^2\,dx + \int_\Omega C|\nabla u|^2\,dx.
\end{aligned}
$$

where we used the fact that there exist positive constants γ and C such that $W''(\xi) \geq \gamma\xi^2 - C$ for all $\xi \in \mathbb{R}$. By (2.18), Lemma 4 applied to u gives:

$$
\int_\Omega u^2|\nabla u|^2\,dx \geq C\int_\Omega u^4\,dx - C\int_\Omega |\nabla u|^2\,dx - C.
$$

Hence,

$$
(I) \leq -C\gamma\int_\Omega u^4\,dx + C\gamma\int_\Omega |\nabla u|^2\,dx + C\gamma. \tag{2.20}
$$

By Hölder's inequality,

$$
\int_\Omega u^4\,dx \geq C\left(\int_\Omega u^2\,dx\right)^2. \tag{2.21}
$$

Combining (2.20) and (2.21) and absorbing γ into the constant C, we get

$$
(I) \leq -C\int_\Omega u^4\,dx - C\left(\int_\Omega u^2\,dx\right)^2 + C\int_\Omega |\nabla u|^2 + C. \tag{2.22}
$$

We now use the following standard interpolation inequality

$$
\int_\Omega |\nabla u|^2\,dx \leq \delta\int_\Omega \Big(\Delta u\Big)^2\,dx + C(\delta)\int_\Omega u^2\,dx.
$$

(where $\delta > 0$ but arbitrarily small) along with (2.22) to obtain the following estimate:

$$
(I) \leq \delta\int_\Omega \Big(\Delta u\Big)^2\,dx - C\int_\Omega u^4\,dx - C\left(\int_\Omega u^2\,dx\right)^2 + C(\delta)\int_\Omega u^2\,dx + C. \tag{2.23}
$$

We turn to estimating (II). Since $f \in C^2(\Omega)$, and since $|W'(\xi)| \leq C\xi^3 + C$, we get

$$
\begin{aligned}
(II) &\leq \delta\int_\Omega \Big(\Delta u\Big)^2\,dx + C\int_\Omega |u|^3\,dx + C \\
&\leq \delta\int_\Omega \Big(\Delta u\Big)^2\,dx + \delta\int_\Omega u^4\,dx + C.
\end{aligned} \tag{2.24}
$$

Putting together our estimates (2.23) for (I) and (2.24) for (II) together with (2.19), we get

$$\begin{aligned}\int_\Omega \Big(\Delta u\Big)^2 dx + \lambda_0 \int_{\Omega\setminus D} (f-u)^2\, dx =& (I) + (II)\\ &\leq \delta \int_\Omega \Big(\Delta u\Big)^2 dx + C(\delta)\int_\Omega u^2\, dx + C\\ &- (C-\delta)\int_\Omega u^4\, dx - C\left(\int_\Omega u^2\, dx\right)^2.\end{aligned}$$

Choosing $\delta > 0$ small enough, one gets

$$\int_\Omega \Big(\Delta u\Big)^2 dx + \lambda_0 \int_{\Omega\setminus D} (f-u)^2\, dx \leq C(\delta)\int_\Omega u^2\, dx - C\Big(\int_\Omega u^2\, dx\Big)^2 + C. \quad (2.25)$$

Let $\xi := \int_\Omega u^2\, dx$. Then the right hand side of (2.25) is $-C\xi^2 + C(\delta)\xi + C$ for some positive constants C. This is a parabola opening downwards, and hence is bounded from above by a constant. That proves the proposition. □

2.3.2 Matching isophotes as λ_0 becomes large

Of interest is what happens to the solution $u(x)$ for the modified Cahn-Hilliard equation when λ_0 is prescribed very large values. Will $u(x)$ correctly match $f(x)$ (the existing image) on the boundary of the inpainting domain? In particular, will the isophote directions be matched? In this section we consider a smooth function f and show that in regions where f changes significantly, the direction of isophotes of the solution will match the direction of isophotes of the prescribed image function. In the next section we extend this result to a binary image with sharp edges. We first establish the following lemma showing that an H^2 steady state solution is actually in $C^{2,\alpha}$. This results is necessary to establish a pointwise bound for the isophotes on the boundary.

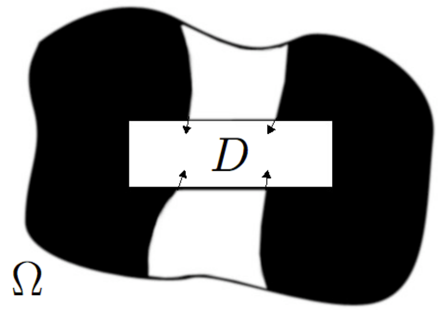

Figure 2.1: Inpainting problem. The isophote vectors are shown.

Lemma 5. *Let Ω have a $C^{2,\alpha}$ boundary and let u be an H^2 weak solution of the PDE*

$$-\Delta\Big(\Delta u - W'(u)\Big) + \lambda(x)(f-u) = 0,$$

where

$$\lambda(x) = \begin{cases} 0 & \textit{if } x \in D, \\ \lambda_0 & \textit{if } x \in \Omega \setminus D \end{cases}$$

Then $u \in C^{2,\alpha}(\Omega)$.

Proof: By assumption, we have that $\lambda(x)(f-u) \in L^2(\Omega)$. Thus $\Delta\Big(\Delta u - W'(u)\Big) \in L^2(\Omega)$ as well. This means that $\Delta u - W'(u) \in H^2(\Omega)$ [Eva98]. Since $u(x,t)$ is bounded in $H^2(\Omega)$ by assumption, it has an a priori pointwise bound, which then implies a pointwise bound on $W'(u)$. Sobolev embedding implies that $u \in C^\alpha(\Omega)$ and thus $W'(u) \in C^\alpha(\Omega)$ for all $0 \leq \alpha < 1$. This implies that $\Delta u \in C^\alpha(\Omega)$, and thus by elliptic regularity [GT83], $u \in C^{2,\alpha}(\Omega)$. $\square$

Remark: The assumptions on smoothness of the boundary are necessary to invoke the theory of elliptic regularity. In practice for many imaging applications, Ω is a square with periodic or reflective boundary conditions. In either of those cases, the domain can be viewed as a manifold without boundary and thus the Lemma is applicable. The details of the boundary would only be important for problems where the inpainting region includes some of the boundary of the image domain.

As part of the proof, we first prove the continuity of ∇u and then show that this leads to matching of the isophote directions in regions where ∇f is large enough. This is sufficient to show continuity of the direction of edges, since they necessarily imply that ∇f is large. We now show that in regions where the image intensity changes, the isophote direction of f matches that of u on ∂D. This is the main theorem for this section.

Theorem 6. *Let Ω satisfy the same conditions as in Lemma 5. Consider isophote directions of f in any region where $|\nabla f| > \delta_0$. The difference of the isophote vectors at the boundary of the inpainting region $\partial(D)$, between the steady state solution to the modified Cahn-Hilliard equation $u(x)$, and the known image $f(x)$, can be made arbitrarily small by choosing λ_0 large enough.*

Proof: Define $g(x) = (u - f)(x)$. First, we would like to show that $\nabla g(x)$ becomes small *pointwise* on $\partial(\Omega \setminus D)$ as λ_0 becomes large. From (2.25) we have that

$$\begin{aligned} \int_\Omega (\Delta g)^2 \, dx &\leq C_1 \\ \int_{\Omega \setminus D} |g(x)|^2 \, dx &\leq \frac{C_2}{\lambda_0} \end{aligned} \tag{2.26}$$

The bounds from 2.26 combined with Sobolev interpolation imply that the $H^{1-\mu}(\Omega \setminus D)$ norm of ∇g is small as $\lambda_0 \to \infty$, for $0 < \mu < \frac{1}{2}$. The restriction map to ∂D (see [Fol95], page 225) implies that ∇g is small in $H^{1/2-\mu}(\partial D)$. Since $L^2(\partial D) \subset H^{1/2-\mu}(\partial D)$ for $0 < \mu < 1/2$, we have that the L^2 norm of ∇g is small on ∂D. Continuity of ∇g implies a pointwise bound on ∇g on the boundary, in particular we have a constant $\eta(\lambda) \to 0$ as $\lambda \to \infty$ such that $|\nabla g||_{\partial D} \leq \eta$. Now we show that this pointwise bound for ∇g implies a bound for the direction of the isophotes.

Let $\frac{\nabla^\perp u}{|\nabla^\perp u|} = \vec{\tau}_u$ (this is the isophote vector). We want to show that $|\vec{\tau}_u - \vec{\tau}_f|$ becomes small on $\partial(\Omega \setminus D)$ as λ_0 takes increasingly large values. Recall that we are only interested in those portions of $\partial(D)$ where $\nabla^\perp f > \delta_0$, with δ_0 small. Some straightforward algebra shows

$$\left|\vec{\tau}_u - \vec{\tau}_f\right| \leq \frac{2|\nabla g|}{\delta_0}. \tag{2.27}$$

Since ∇g is small for large λ_0, we have the desired result. The case where $\nabla^\perp f \leq \delta_0$ is not interesting, for in these regions the image is nearly constant and thus does not produce any significant edges. This completes the proof of Theorem 6. □

2.4 Matching of isophotes for binary images: continuity of the edge direction

The previous analysis considered the modified Cahn-Hilliard equation (2.1) with $\varepsilon = 1$. In real applications involving binary images, we take ε small as it defines a diffuse interface thickness. Our previous estimates are for smooth functions f and in order to apply these ideas, we regularize a binary f at the same scale as the diffuse interface thickness ε. We state this problem as follows: consider a binary image function f taking values 0 and 1. Assume a smooth boundary between regions where $f = 0$ and $f = 1$. Using a mollifier, construct $f_\varepsilon = J_\varepsilon f(x)$. A simple way to do this is to solve the heat equation on Ω, with Neumann boundary conditions and initial condition f, until time $t = \varepsilon^2$. This gives a smooth approximation of f in which the edges of the images are smoothed over a scale of length ε.

We now solve the inpainting problem by evolving the time dependent equation

$$u_t = -\Delta\left(\varepsilon\Delta u - \frac{1}{\varepsilon}W'(u)\right) + \lambda(x)(f_\varepsilon - u). \tag{2.28}$$

where

$$\lambda(x) = \begin{cases} 0 & \text{if } x \in D, \\ \lambda_0 & \text{if } x \in \Omega \setminus D. \end{cases}$$

Global existence of a weak solution of the above problem follows from the arguments in section 4. We now consider the steady state problem

$$-\Delta\left(\varepsilon\Delta u - \frac{1}{\varepsilon}W'(u)\right) + \lambda(x)(f_\varepsilon - u) = 0 \tag{2.29}$$

where

$$\lambda(x) = \begin{cases} 0 & \text{if } x \in D, \\ \lambda_0 & \text{if } x \in \Omega \setminus D, \end{cases}$$

and follow the arguments of the preceding section to show that for sufficiently large λ_0, the steady state solution above has edges matching those of the original image f. To do this, we show that for a fixed ε, λ can be chosen large enough so that the isophote directions are nearly parallel on the boundary of D.

We consider the analogous estimates to (2.17) for the case $\varepsilon \neq 1$. Take the inner produce of the steady state equation with $(u - f)$. We obtain

$$\varepsilon\int_\Omega (\Delta u)^2\,dx + \int_{\Omega\setminus D} \lambda_0(f-u)^2 = \frac{1}{\varepsilon}\int_\Omega W'(u)\Delta u\,dx + \int_\Omega (\varepsilon\Delta u - \frac{1}{\varepsilon}W'(u))\Delta f\,dx. \tag{2.30}$$

This in turn leads to the estimate

$$\begin{aligned}\varepsilon\int_\Omega \Big(\Delta u\Big)^2 dx + \lambda_0\int_{\Omega\setminus D}(f-u)^2\,dx =& (I) + (II)\\ &\le (\varepsilon + \frac{1}{\varepsilon})\delta\int_\Omega \Big(\Delta u\Big)^2 dx + \frac{1}{\varepsilon}C(\delta)\int_\Omega u^2\,dx + C(\frac{1}{\delta}, \varepsilon + \frac{1}{\varepsilon})\\ &\quad - \frac{1}{\varepsilon}(C-\delta)\int_\Omega u^4\,dx - \frac{1}{\varepsilon}C\left(\int_\Omega u^2\,dx\right)^2.\end{aligned} \tag{2.31}$$

Now letting δ become very small, as ε is fixed, we have that

$$\varepsilon \int_\Omega \Big(\Delta u\Big)^2 dx + \lambda_0 \int_{\Omega\setminus D} (f-u)^2\, dx \le -\frac{1}{\varepsilon} C\Big(\int_\Omega u^2\, dx\Big)^2 + \frac{1}{\varepsilon} C \int_\Omega u^2\, dx + C(\varepsilon + \frac{1}{\varepsilon}). \tag{2.32}$$

Once again, the right hand side of the inequality is a parabola that opens downward. Thus:

$$\varepsilon \int_\Omega \Big(\Delta u\Big)^2 dx + \lambda_0 \int_{\Omega\setminus D} (f-u)^2\, dx \le C(\varepsilon + \frac{1}{\varepsilon}), \tag{2.33}$$

from which we obtain the bounds

$$\begin{aligned} \textstyle\int_\Omega \Big(\Delta u\Big)^2 dx \ &\le\ C((\varepsilon + \tfrac{1}{\varepsilon})\tfrac{1}{\varepsilon}), \\ \textstyle\int_{\Omega\setminus D} (f-u)^2\, dx \ &\le\ \tfrac{C(\varepsilon+\frac{1}{\varepsilon})\frac{1}{\varepsilon}}{\lambda_0}. \end{aligned} \tag{2.34}$$

This shows the full relationship between λ_0 and ε. It is important to notice that the constants $C(\frac{1}{\varepsilon^2})$ and $C(\varepsilon + \frac{1}{\varepsilon})$ become very large as ε becomes small. Thus, for small ε, λ_0 must be chosen very large to guarantee continuity of edges using these estimates.

Using the results of section 2.3, we have that $\nabla(u - f_\varepsilon)(x) \to 0$ on ∂D as $\lambda_0 \to \infty$. Consider now the part of ∂D where $|\nabla f_\varepsilon| > \delta_0$. Since the original f is binary, this region corresponds to a narrow band around the edges of the original f. Following the ideas in section 2.4, we see that the isophote vectors $|\vec{\tau}_u - \vec{\tau}_{J_\varepsilon f}| \to 0$ in this narrow band which defines the diffuse interface between regions where $f = 0$ and $f = 1$. Putting this all together, we consider an original f taking values 0 and 1 with smooth boundary between the two phases. Assume that ε is small enough so that τ_{f_ε} is almost parallel to the edge direction of the original binary f in the region where $|\nabla f_\varepsilon| > \delta_0$. The solution u of the steady state diffuse interface problem will have edges that line up with those of f_ε and thus with the original binary f, provided that λ_0 is large enough (depending on our choice of ε).

In the above discussion, we implicitly assume a 'separation of scales' in the solution u. If we assume f is a binary image with order one features and curvature of edges, then the regularized f_ε is guaranteed to have a separation of scales, meaning that it consists of regions separated by diffuse interfaces where there is steep variation (on a spatial scale on order ε) normal to the diffuse interface and very mild variation tangent to the interface direction. If the solution u_ε has the same separation of scales as the regularized data f_ε, then the result will be a matching of edges between the data and the solution, for large λ. Note that the estimates derived above require λ to possibly be very large, depending badly on ε. In our analysis here we do not prove that a separation of scales occurs for the solution u in the inpainting region, however the computational results of chapter 4 illustrate this to be the case. Such a result is beyond the scope of this thesis but would be interesting to examine in its own right. The original asymptotic analysis for separation of scales for the plain Cahn-Hilliard equation was carried out by Pego [Peg89]. The analysis is local and thus should hold in the interior of the inpainting region where the fidelity term is zero. Our simulations are observed to follow the same scaling as the original Cahn-Hilliard equation, in the inpainting region. In chapter 4, we present numerical results illustrating that separation of scales for u, and thus continuation of edge direction, does occur for this model. See in particular figures 4.2-4.11.

In addition to having two spatial scales, the original Cahn-Hilliard asymptotics shows separation of time scales. There is a short time scale on which phase separation occurs, and a longer time scale (related to ε) on which the diffuse interface boundary moves. These same time scales are present in our modified equation. In the analysis above we consider the steady state problem. In the numerical examples, λ is chosen large enough so that the 'fidelity timescale' is short compared to the other timescales in the problem associated with the regular Cahn-Hilliard dynamics. The timescale associated with the motion of the interface must be addressed when designing fast algorithms for binary inpainting. In chapter 8 we make use of this separation of timescales to design a two-step algorithm in which reconnection of shapes is first performed with a large ε, thereby decreasing the timescale of reconnection. Then we suddenly decrease ε to sharpen the interface, which also happens on a short timescale as this dynamics is associated with phase separation rather than interface motion. The need for a two-step method is further explained by the stripe reconnection examples in the following section. There we compute bifurcation diagrams for steady states associated with a single stripe reconnection. For a large gap width, the connected stripe solution is a separate branch from the branch of solutions that contains the stable solution for large ε. We explain this in more detail in the following section.

2.5 Bifurcations of the modified Cahn-Hilliard equation

A natural question to ask is whether the steady state solution is unique. Here we show by numerical examples that multiple solutions exist and can be understood through a bifurcation analysis. We conducted tests of the modified Cahn-Hilliard equation

$$u_t = -\Delta\Big(\varepsilon\Delta u - \frac{1}{\varepsilon}W'(u)\Big) + \lambda_0(f - u)\chi_{\Omega\setminus D} \tag{2.35}$$

on a simple stripe geometry. The numerical scheme used is based on convexity splitting and is discussed in detail in chapter 3 (see also [BEGar, VR03]). Figure 2.2 shows an example where the inpainting domain D is the gray region in frame (a). Different initial conditions for the dynamic problem (2.35) yield different steady state solutions as shown in frames (b) and (c). In both examples we take the same initial condition $u_0 = f$ in $\Omega \setminus D$ and $u_0 = 0$ in D. However, in the case of (b) we start with a large $\varepsilon = 0.8$, run the solution to steady state, and use this as a new initial condition for a smaller value of ε. In the case (c) we perform a single simulation with fixed ε small (0.01), starting from u_0 given above. We can not take ε much smaller without having to increase the resolution of the grid. In practice, the Cahn-Hilliard dynamics is reasonably well-captured with a few grid points resolving the diffuse interface scale ε [Gla03, VR03]. A much coarser grid can result in numerical pinning of the interface.

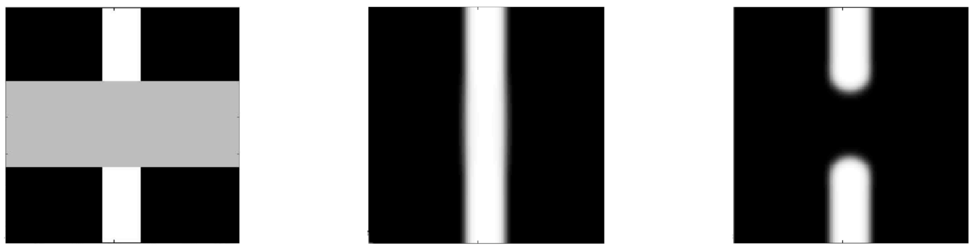

(a) (b) (c)

Figure 2.2: (a) Gray portion denotes the inpainting region D while the black and white portion denote the background image f. (b) Steady state solution of (2.35) showing a completed stripe. (c) Steady state solution of (5.7) showing a broken stripe. In both cases $\varepsilon = 0.01$. In all cases we choose a square of 128×128 grid points, with the inpainting region having a gap of width 40 grid points. The grid spacing is $\Delta x = 0.01$.

The bifurcation diagrams below in figure 2.3 show how the steady states, for the modified Cahn-Hilliard equation, change in response to changes in the value of ε. We consider the stripe problem as above, for different gap widths of 30, 45, and 80. We choose an amplitude for the bifurcation diagrams of the value of the steady state solution at the center of the inpainting domain D. This is a useful measure in that a completed stripe will have an amplitude close to one, whereas a broken stripe will have an amplitude close to zero. Intermediate values are observed for steady states in which the diffuse interface scale ε is comparable to the feature size in the problem.

Note that in all figures, only stable steady states are shown, as we use the time

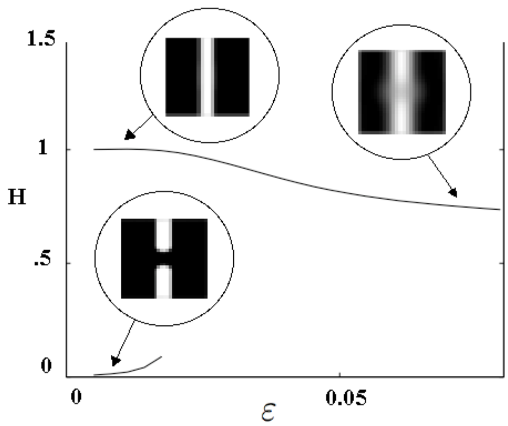

(a)

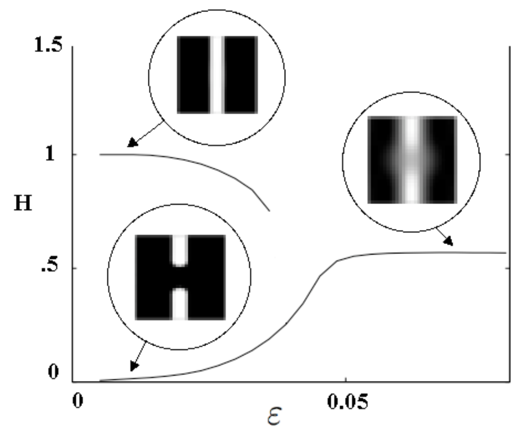

(b)

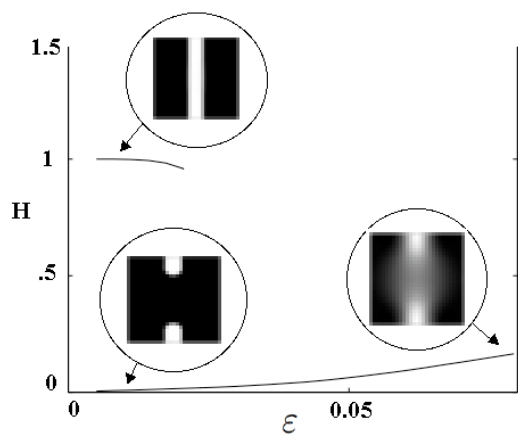

(c)

Figure 2.3: Bifurcation diagrams for, (a) gap of 30, (b) gap of 45, (c) gap of 80. The y-axis shows the steady state height of the midpoint of the stripe, while the x-axis is the epsilon value. The steady states are shown visually in thumbnails, with an arrow pointing to their positions on the respective bifurcation diagrams. Only stable steady states are shown.

dependent PDE to obtain the steady states. These figures suggest the presence of an incomplete pitchfork bifurcation. A diagram for this type of bifurcation is shown in figure 2.4 [Str94] in which stable branches appear as solid lines and unstable branches appear as dotted lines. Frame (b) shows the classical complete pitchfork bifurcation. Changes in parameters, including, but not limited to symmetry breaking, can cause a section of the pitchfork to break off into a stable/unstable pair of solutions, as shown in frames (a) and (c). It is interesting to compare the diagram in figure 2.4 with the numerically obtained diagrams in figure 2.3. In frame (a) there is an unbroken stable branch connecting the single large ε solution to the connected stripe solution for small ε. In contrast, in frames (b) and (c), the unbroken stable branch connects the single large ε solution to the broken stripe solution for small ε. In these cases the connected stripe solution appears as an isolated branch. We conjecture that the isolated branch flips over to an unstable branch of steady state solutions in all three cases. In frame (a) it is the broken stripe solution that forms an isolated branch.

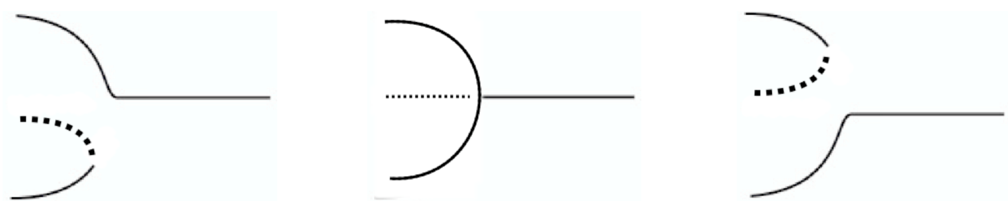

(a) (b) (c)

Figure 2.4: Bifurcation diagrams relating to the phenomena shown in figure 2.3. (a) An incomplete pitchfork bifurcation. (b) A symmetric pitchfork bifurcation. (c) Another incomplete pitchfork bifurcation.

The bifurcation diagrams above suggest that different approaches will be necessary to obtain the completed stripe solution, depending on the gap width. For the small gap case, one can simply compute the steady state at large ε and continuously shrink ε, following the stable branch, to the desired small ε. However this approach will clearly not work for the larger gap widths. Instead, we find that a two-scale approach empirically works well to obtain the continued stripe solution. We choose, at the outset, a value of ε on the order of the maximum gap size. For example, choosing $\varepsilon = .8$ as a starting value, we find a unique steady state solution for a very diffuse scale. Instead of continuously lowering ε, we abruptly change to the desired small scale value and find empirically that the continued stripe solution emerges from the dynamics. In summary, our algorithm for finding the completed stripe solutions is as follows:

1. Choose an initial value of ε nearly equal to the numerical maximum gap spacing (above $\varepsilon = .8$ was used). Set $\Delta t = 1$, with $\Delta x = \Delta y = .01$. The image size is taken to be 128×128 grid points, each of size Δx.

2. Run the modified Cahn-Hilliard equation to near steady state (300 iterations) for this value of ε.

3. At 300 iterations, multiply the near steady state solution $u(x, y)$ by a factor more than 1 so that $\max[u(x, y)] = 1.0$.

4. Still at 300 iterations, switch ε to a value of .01 (approximately the numerical grid spacing value Δx).

In practice, to obtain the steady state requires less than 30 seconds on a Pentium 4 processor. Figure 2.5 (a), (b), (c), shows an example of such a calculation.

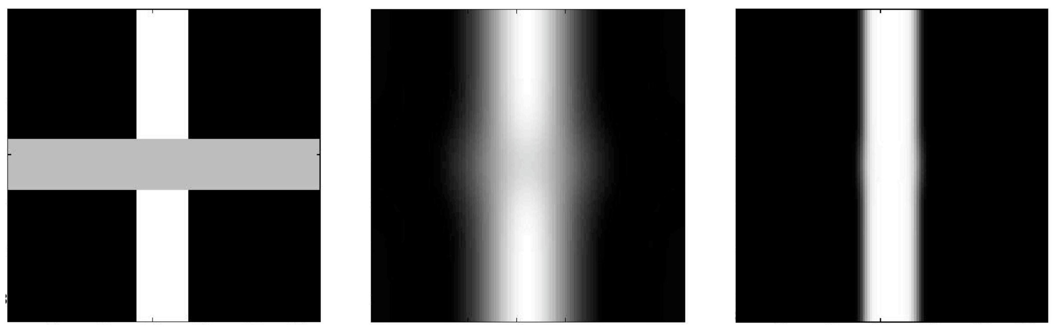

(a) (b) (c)

Figure 2.5: Disconnected stripe with a gap of 20, at (a) t=0, (b) t=299, after steady state had been reached for $\varepsilon = .8$, (c) t=500 (produced by switching to $\varepsilon = .01$ at t = 300).

CHAPTER 3

Numerical Algorithm

In this chapter we demonstrate how to implement Cahn-Hilliard inpainting using a specific fast solver known as *convexity splitting* [BEGar, Eyr98, VR03]. However, other fast solvers might be used with good performance. Convexity splitting involves dividing up the energy functional for the equation into two parts – a convex energy plus a concave energy. The part of the Euler-Lagrange equation derived from the convex portion is then treated implicitly in the numerical scheme, while the portion derived from the concave part is treated explicitly.

Under the right conditions, convexity splitting for gradient flow-derived equations can allow for an unconditionally gradient stable time-discretization scheme, which means arbitrarily large time steps can be taken. Vollmayr-Lee and Rutenberg [VR03] have more recently refined the conditions under which stability is applicable for the traditional Cahn-Hilliard equation.

This method has been investigated previously for the case of fourth order partial differential equations by Greer, et al [GBS06]. Elsewhere, Hsiang-Wei Lu et al [LKK05] and K. Glasner [Gla03] have used convexity splitting to approach the solution of the Hele-Shaw equation.

3.1 Convexity splitting algorithm for the modified Cahn-Hilliard equation

The new modified Cahn-Hilliard equation is not strictly a gradient flow. The original Cahn-Hilliard equation (1.36) is indeed a gradient flow using an H^{-1} norm for the energy

$$E_1 \;=\; \int_\Omega \frac{\varepsilon}{2}|\nabla u|^2 + \frac{1}{\varepsilon}W(u)\; d\vec{x}, \tag{3.1}$$

while the fidelity term in the modified Cahn-Hilliard equation (2.35) can be derived from a gradient flow under an L^2 norm for the energy

$$E_2 \;=\; \lambda_0 \int_{\Omega\backslash D} (f-u)^2 d\vec{x}. \tag{3.2}$$

This has been discussed in chapter 2. Again, in total, the modified Cahn-Hilliard equation is neither a gradient flow in H^{-1} nor L^2. However, the idea of convexity splitting, one for the Cahn-Hilliard energy in equation (3.1) and one for the energy E_2 in equation (3.2), can still be applied to this problem with good results.

For example, one can split E_1 as

$$E_1 \;=\; E_{11} \;-\; E_{12} \tag{3.3}$$

where

$$E_{11} = \int_\Omega \frac{\varepsilon}{2}|\nabla u|^2 + \frac{C_1}{2}|u|^2\; d\vec{x}, \tag{3.4}$$

and

$$E_{12} \;=\; \int_\Omega -\frac{1}{\varepsilon}W(u) + \frac{C_1}{2}|u|^2\; d\vec{x}. \tag{3.5}$$

A possible splitting for E_2 is

$$E_2 \;=\; E_{21} \;-\; E_{22} \tag{3.6}$$

where

$$E_{21} = \int_{\Omega\setminus D} \frac{C_2}{2}|u|^2 \, d\vec{x}, \tag{3.7}$$

and

$$E_{22} = \int_{\Omega\setminus D} -\lambda_0(f-u)^2 + \frac{C_2}{2}|u|^2 \, d\vec{x}. \tag{3.8}$$

For the splittings discussed above, the resulting time-stepping scheme is:

$$\frac{u^{n+1}-u^n}{\Delta t} = -\nabla_{H^{-1}}(E_{11}^{n+1} - E_{12}^n) - \nabla_{L^2}(E_{21}^{n+1} - E_{22}^n), \tag{3.9}$$

where $\nabla_{H^{-1}}$ and ∇_{L^2} represent gradient descent with respect to the H^{-1} inner product, and L^2 inner product, respectively. This translates to a numerical scheme of the form

$$\begin{aligned}\frac{u^{n+1}(\vec{x}) - u^n(\vec{x})}{\partial t} &+ \varepsilon\Delta^2 u^{n+1}(\vec{x}) - C_1\Delta u^{n+1}(\vec{x}) + C_2 u^{n+1}(\vec{x}) \\ &= \Delta(\frac{1}{\varepsilon}W'(u^n(\vec{x}))) + \lambda(\vec{x})(f(\vec{x}) - u^n(\vec{x})) \\ &\quad - C_1\Delta u^n(\vec{x}) + C_2 u^n(\vec{x}).\end{aligned} \tag{3.10}$$

The constants C_1 and C_2 are positive, and need to be chosen large enough so that the energies E_{11}, E_{12}, E_{21}, and E_{22} are convex. Thus, C_1 should be comparable to $\frac{1}{\varepsilon}$, while C_2 should be comparable to λ_0 (this can be seen from equations (3.5) and (3.7)). Numerical tests have shown that with these choices the scheme (3.10) becomes unconditionally stable. Equation (3.10) is then solved for $u^{n+1}(\vec{x})$, given $u^n(\vec{x})$, by way of a two-dimensional Fast-Fourier-Transform method.

3.2 Fourier spectral method used for computation

The one-dimensional discrete Fourier Transform is defined as follows (see, for example, [Str89], pages 38-40):

$$(u_i)\hat{}(k) = \sum_{i=0}^{N-1} u_i e^{-2\pi I \frac{i}{N} k} \frac{1}{N}, \tag{3.11}$$

where we have used I to denote the imaginary number i to avoid confusion with indexes. Notice this definition is for N grid points numbered 0 to $N-1$. We will use equation (3.11) as a starting point to find the discrete Fourier Transform of our numerical scheme shown in equation (3.10).

We begin with the following definitions:

$$\begin{aligned}
D_i^+ u_{i,j} &= \frac{u_{i+1,j} - u_{i,j}}{h} \\
D_i^- u_{i,j} &= \frac{u_{i,j} - u_{i-1,j}}{} \\
D_j^+ u_{i,j} &= \frac{u_{i,j+1} - u_{i,j}}{h} \\
D_j^- u_{i,j} &= \frac{u_{i,j} - u_{i,j-1}}{h}
\end{aligned} \tag{3.12}$$

where h is the numerical grid spacing, which we have set to $h = \frac{1}{N}$.

We then form Riemann sums to find the discrete Fourier Transforms of equation (3.12). For example, for the $D_i^+ u_{i,j}$, the discrete Fourier Transform is:

$$(D_i^+ u_{i,j})\hat{}(k) = \sum_{i=0}^{N-1} \frac{u_{i+1,j}}{\frac{1}{N}} e^{-2\pi I \frac{i}{N} k} \frac{1}{N} \;-\; \sum_{i=0}^{N-1} \frac{u_{i,j}}{\frac{1}{N}} e^{-2\pi I \frac{i}{N} k} \frac{1}{N} \tag{3.13}$$

and by manipulating the index i, we get:

$$(D_i^+ u_{i,j})\hat{}(k) = (e^{2\pi I \frac{k}{N}} - 1) \sum_{i=1}^{N-1} \frac{u_{i,j}}{\frac{1}{N}} e^{-2\pi I \frac{i}{N} k} \frac{1}{N} + u_{N,j} - u_{0,j} \tag{3.14}$$

but for the case of a periodic domain, we have that

$$u_{N,j} = u_{0,j} \tag{3.15}$$

so that finally we get

$$(D_i^+ u_{i,j})\hat{}(k) = \frac{(e^{2\pi I \frac{k}{N}} - 1)}{\frac{1}{N}} \sum_{i=1}^{N-1} u_{i,j} e^{-2\pi I \frac{i}{N} k} \frac{1}{N} \tag{3.16}$$

When the second dimension is taken into account, we find:

$$(D_i^+ u_{i,j})\hat{}(k,l) = \frac{(e^{2\pi I \frac{k}{N}} - 1)}{\frac{1}{N}} \sum_{i=1}^{N-1} \sum_{j=1}^{N-1} u_{i,j} e^{-2\pi I \frac{i}{N} k} e^{-2\pi I \frac{i}{N} l} \frac{1}{N^2} \tag{3.17}$$

Likewise, we find that:

$$(D_i^- u_{i,j})\hat{}(k,l) = \frac{(1 - e^{-2\pi I \frac{k}{N}})}{\frac{1}{N}} \sum_{i=1}^{N-1} \sum_{j=1}^{N-1} u_{i,j} e^{-2\pi I \frac{i}{N} k} e^{-2\pi I \frac{i}{N} l} \frac{1}{N^2}$$

$$(D_j^+ u_{i,j})\hat{}(k,l) = \frac{(e^{2\pi I \frac{l}{N}} - 1)}{\frac{1}{N}} \sum_{j=1}^{N-1} \sum_{i=1}^{N-1} u_{i,j} e^{-2\pi I \frac{i}{N} k} e^{-2\pi I \frac{i}{N} l} \frac{1}{N^2}$$

$$(D_j^- u_{i,j})\hat{}(k,l) = \frac{(1 - e^{-2\pi I \frac{l}{N}})}{\frac{1}{N}} \sum_{j=1}^{N-1} \sum_{i=1}^{N-1} u_{i,j} e^{-2\pi I \frac{i}{N} k} e^{-2\pi I \frac{i}{N} l} \frac{1}{N^2} \tag{3.18}$$

Continuing,

$$(D_i^- D_i^+ u_{i,j})\hat{}(k,l) = \frac{(e^{-2\pi I \frac{k}{N}} + e^{2\pi I \frac{k}{N}} - 2)}{(\frac{1}{N})^2} \sum_{i=1}^{N-1} \sum_{j=1}^{N-1} u_{i,j} e^{-2\pi I \frac{i}{N} k} e^{-2\pi I \frac{l}{N} l} \frac{1}{N^2}$$

$$(D_j^- D_j^+ u_{i,j})\hat{}(k,l) = \frac{(e^{-2\pi I \frac{l}{N}} + e^{2\pi I \frac{l}{N}} - 2)}{(\frac{1}{N})^2} \sum_{j=1}^{N-1} \sum_{i=1}^{N-1} u_{i,j} e^{-2\pi I \frac{i}{N} k} e^{-2\pi I \frac{l}{N} l} \frac{1}{N^2} \tag{3.19}$$

and then finally the discrete Laplacian is

$$(\Delta_{i,j} u_{i,j})\hat{}(k,l) = \frac{(e^{-2\pi I \frac{k}{N}} + e^{2\pi I \frac{k}{N}} + e^{-2\pi I \frac{l}{N}} + e^{2\pi I \frac{l}{N}} - 4)}{(\frac{1}{N})^2} \sum_{i=1}^{N-1} \sum_{j=1}^{N-1} u_{i,j} e^{-2\pi I \frac{i}{N} k} e^{-2\pi I \frac{l}{N} l} \frac{1}{N^2}. \tag{3.20}$$

Or more simply,

$$(\Delta_{i,j} u_{i,j})\hat{}(k,l) = (e^{-2\pi I \frac{k}{N}} + e^{2\pi I \frac{k}{N}} + e^{-2\pi I \frac{l}{N}} + e^{2\pi I \frac{l}{N}} - 4) N^2 \text{ fft2}(u_{i,j}), \tag{3.21}$$

and the coefficients of the Laplacian are:

$$M_{k,l} = (e^{-2\pi I \frac{k}{N}} + e^{2\pi I \frac{k}{N}} + e^{-2\pi I \frac{l}{N}} + e^{2\pi I \frac{l}{N}} - 4)$$

where the MATLAB function "fft2" is used to represent the two-dimensional discrete Fourier Transform of the matrix $u_{i,j}$. Note that both k and l run from 0 to $N - 1$.

Recall our numerical scheme for the modified Cahn-Hilliard equation above:

$$\begin{aligned}\frac{u^{n+1}(\vec{x})-u^n(\vec{x})}{\delta t}&+\varepsilon\Delta^2 u^{n+1}(\vec{x})-C_1\Delta u^{n+1}(\vec{x})+C_2u^{n+1}(\vec{x})\\&=\Delta(\frac{1}{\varepsilon}W'(u^n(\vec{x})))+\lambda(\vec{x})(f(\vec{x})-u^n(\vec{x}))\\&\quad-C_1\Delta u^n(\vec{x})+C_2u^n(\vec{x}).\end{aligned}\tag{3.22}$$

To evaluate the Laplacian and bi-Laplacian operators numerically, we use the discrete Fourier spectral method just outlined. We separate the u^{n+1} terms from the u^n terms, placing them on separate sides of the equation:

$$\begin{aligned}u^{n+1}(\vec{x})&+\varepsilon\Delta^2 u^{n+1}(\vec{x})-C_1\Delta u^{n+1}(\vec{x})+C_2u^{n+1}(\vec{x})\\&=\delta t\Big[\Delta(\frac{1}{\varepsilon}W'(u^n(\vec{x})))+\lambda(\vec{x})(f(\vec{x})-u^n(\vec{x}))\\&\quad-C_1\Delta u^n(\vec{x})+C_2u^n(\vec{x})\Big]+u^n(\vec{x}).\end{aligned}\tag{3.23}$$

Taking the Fourier Transform of both sides (note that $u^n(\vec{x})$ is identical to $u^n_{i,j}$ from above), we have that

$$\begin{aligned}(1\ &+\varepsilon M_{k,l}^2-C_1M_{k,l}+C_2)\hat{u}^{n+1}(k,l)\\&=\delta t\Big[M_{k,l}\Big(\frac{1}{\varepsilon}W'(u^n)\Big)^\wedge(k,l)\ +\Big(\lambda(\vec{x})(f(\vec{x})-u^n(\vec{x}))\Big)^\wedge(k,l)\\&\quad-C_1M_{k,l}\hat{u}^n(k,l)+C_2\hat{u}^n(k,l)\Big]+\hat{u}^n(k,l).\end{aligned}\tag{3.24}$$

Solving for $\hat{u}^{n+1}$, this simplifies to

$$\hat{u}^{n+1}(k,l)=\frac{\delta tM_{k,l}\Big[\frac{1}{\varepsilon}\Big((W')(u^n)\Big)^\wedge(k,l)\ -C_1\hat{u}^n(k,l)\Big]+\delta t\Big[\lambda(\vec{x})f(\vec{x})+(C_2-\lambda(\vec{x}))u^n(\vec{x})\Big]^\wedge(k,l)\ +\hat{u}^n(k,l)}{1+\varepsilon M_{k,l}^2-C_1M_{k,l}+C_2}\tag{3.25}$$

As the individual discrete Fourier Transforms on the right side of equation (3.25) are easy to calculate given u^n, this method rapidly and effectively calculates the matrix $\hat{u}^{n+1}$. All that remains is then to compute the inverse discrete Fourier Transform on $\hat{u}^{n+1}$, which is defined to be (see for example [Str89]):

$$u_{i,j}^{n+1} = \sum_{k=1}^{N-1} \sum_{l=1}^{N-1} \hat{u}^{n+1}(k,l) e^{2\pi I \frac{k}{N} i} e^{2\pi I \frac{l}{N} j} \frac{1}{N^2}. \tag{3.26}$$

In the next chapter, we present some examples in which we indicate precise values of Δt, C_i, λ, and ε (see equation (3.10)) used to perform the inpainting.

CHAPTER 4

Results

The modified Cahn-Hilliard equation lends itself particularly well to the inpainting of simple binary shapes, such as stripes and circles. Moreover, its applicability can be extended to achieve inpainting of objects composed of stripes and circles, i.e., roads or text. Below and on the next page, we show several examples of the method and its performance. All examples were performed on a Linux desktop system using a Pentium 4 processor, and programmed in MATLAB. Further details can be found in our papers [BEGar], and [BEG06]. Unless otherwise denoted, all times are given as number of iterative steps of the numerical algorithm (i.e., $t = 50$ means the 50th step of the numerical scheme detailed in chapter 3).

4.1 Inpainting of a double stripe

Above in figure 4.1, we see the two-step process at work to inpaint two stripes. The gray region in figure 4.1(a) denotes the inpainting region. We begin running the modified Cahn-Hilliard equation with a large value of ε $(= .8)$, and at $t = 50$ we reach a steady state. We then switch to a small value of ε $(= .01)$, using the result from figure 4.1(b) as initial data. The final result is reached at $t = 700$ and is shown in figure 4.1(c). In this test, Δt was set to 1, $\lambda = 50,000$, $C_1 = 300$, and $C_2 = 150,000$.

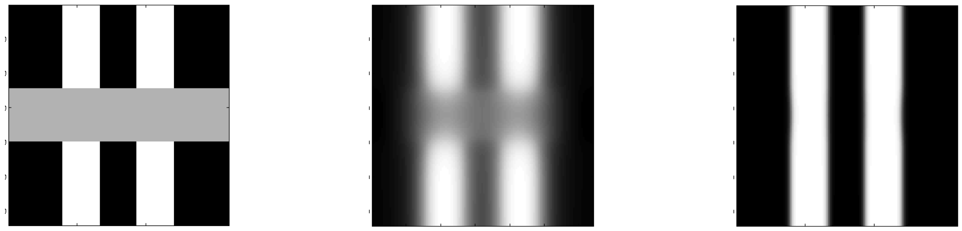

(a) (b) (c)

Figure 4.1: (a) Initial data (inpainting region in gray). (b) Intermediate state at $t = 50$. (c) steady state at $t = 700$. (Gap distance is 30 units, Image domain is 128×128).

4.2 Inpainting of a cross

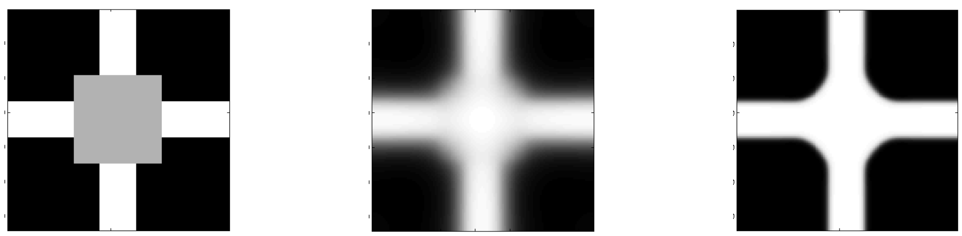

(a) (b) (c)

Figure 4.2: (a) Initial data of cross (inpainting region in gray). (b) Intermediate state at $t = 300$. (c) Steady state at $t = 1000$. (Image domain is 128×128, stripe width is 20 units, initial gap distance is 50 units).

In figure 4.2(a), the gray region denotes the "gap", or region to be inpainted. As with the stripes, the modified Cahn-Hilliard equation is run to steady state for a large value of ε (= .8), resulting in figure 4.2(b) at $t = 300$. This data is then used as initial data for the modified Cahn-Hilliard equation with ε (= .01) set to a small value. The final result is a completed cross at $t = 1000$. The parameters were set as $\Delta t = 1$, $\lambda = 100,000$, $C_1 = 300$, and $C_2 = 3\lambda$.

4.3 Inpainting across large gaps

In figure 4.3, a stripe is bridged across a gap that is 20 times as long as the stripe is wide.

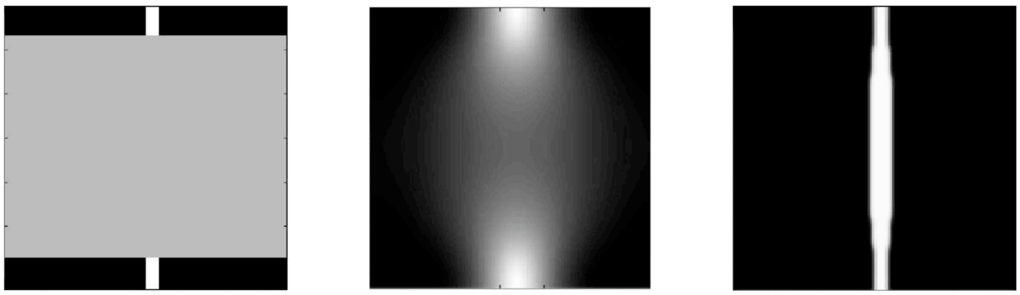

(a) (b) (c)

Figure 4.3: (a) Initial data (inpainting region in gray). (b) Intermediate state at $t = 499$. (c) near steady state at $t = 8000$. (Gap distance is 100 units, and the stripe width is 5 units. Image domain is 128×128.)

4.4 Inpainting of a sine wave

Figure 4.4 shows how the modified Cahn-Hilliard equation may be applied to the inpainting of simple road-like structures. In figure 4.4(a), an incomplete sine wave is shown. In figure 4.4(b), the sine wave is artificially "fattened" by expanding each white point's area radially by a factor of 3. This is done in order to give the modified Cahn-Hilliard equation sufficient boundary conditions to do effective inpainting.

In figure 4.4(c), the gray area represents the inpainting region. The remaining white and black portions of the image are thus outside the inpainting region, and essentially held fixed in place by the fidelity term of the modified Cahn-Hilliard equation (2.35). The two-step method was then used to inpaint the sine wave.

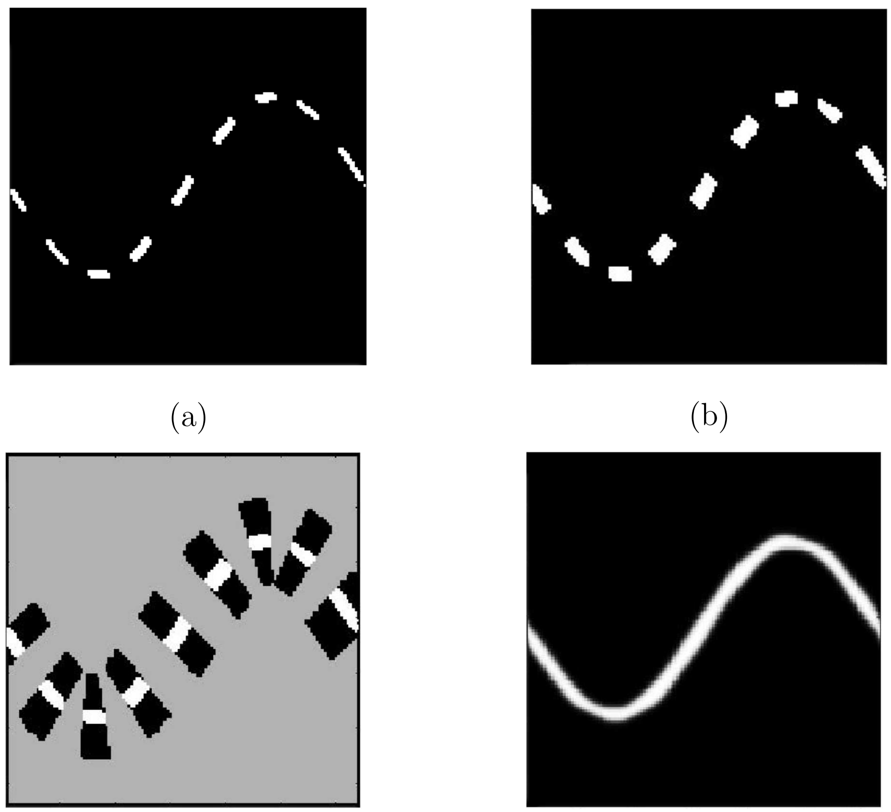

(a) (b) (c) (d)

Figure 4.4: Inpainting a sine wave. (Image domain is 128×128).

Figure 4.4(d) shows the finished result.

The initial value of ε was taken to be .8, and then at $t = 200$ this was switched to a value of $\varepsilon = .01$. The final inpainting result was taken at $t = 4000$ (which corresponds to a time of 24 seconds real processing time). The parameters were set as: $\lambda = 100,000$, $\Delta t = 1$, $C_1 = 300$, and $C_2 = 3\lambda$.

4.5 Inpainting of a road

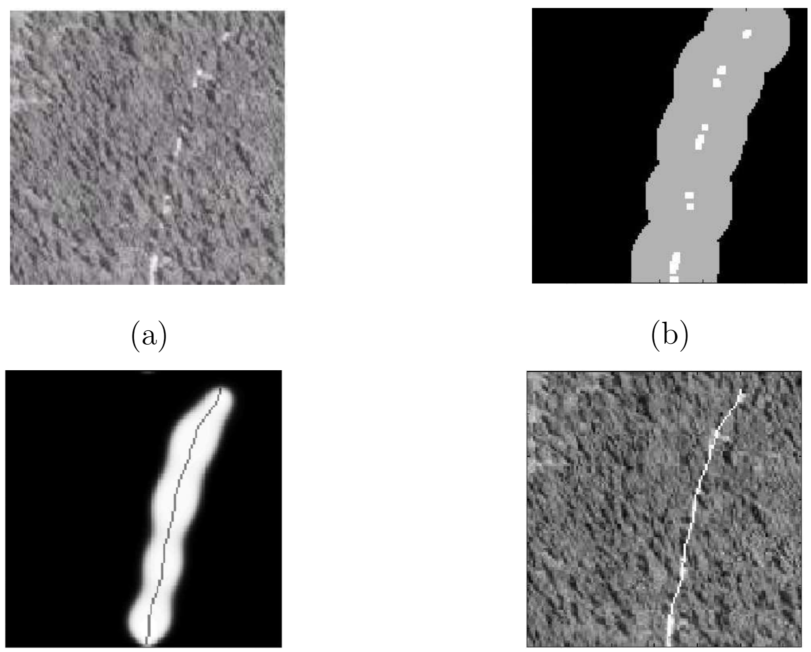

(a) (b)

(c) (d)

Figure 4.5: Inpainting of an obscured road. (Image domain is 128×128).

Figure 4.5(a) shows a satellite image of a road passing through a forest in Washington state. After a simple thresholding of grayscale values, the visible pieces of the road are shown as the white regions in figure 4.5(b). The gray area in figure 4.5(b) represents the inpainting region, which was found by creating a circle about each established point of the road, the radius of which was chosen to be the maximum estimated gap length between existing portions of the road.

Note also that each thresholded white point of the road has been expanded in radius, as was done for the sine wave in figure 4.4(b). In the original satellite photo, the road actually has an average width of about 1 pixel, making it very difficult to establish meaningful boundary conditions for the inpainting problem.

In figure 4.5(c), steady state has been reached using the modified Cahn-Hilliard equation, via the aforementioned two-step process. The result in (c) is too thick, but if a centerline extraction is performed, and the resulting centerline overlaid on the initial satellite photo, we arrive at an estimation of the path of the road through the trees as shown in figure 4.5(d). Note that the result in figure 4.5(d) does not continue the road to the top of the satellite photo. This is due to a lack of data for the road in that region, as exemplified by figure 4.5(b).

The initial value for ε was .8, which was switched at $t = 100$ to $\varepsilon = .005$. The final result was taken at $t = 500$ (which corresponds to 6 seconds of processor time). The parameters were: $\Delta t = 1$, $\lambda = 1,000,000$, $C_1 = 30,000$, and $C_2 = 3\lambda$.

Much more efficient inpainting, akin to what was accomplished for the sine wave in figure 4.4 could be done, if a smaller inpainting region could be determined. For example, the reason that figure 4.5(c) displays such a poor representation of a road is due to the inpainting region literally being too wide (the gray portion of figure 4.5(b)). If we could come up with an inpainting region similar to that in figure 4.4(c), much better approximations to the road could be accomplished, possibly negating the need for centerline extraction.

(a)

(b)

Figure 4.6: Recovery of damaged text. (Image domain was 128×128).

(a)

(b)

Figure 4.7: Recovery of damaged text. (Image domain was 256×256).

4.6 Recovery of text

In figure 4.6(a), several lines obscure some Arabic writing. Using these obstructing lines as the inpainting region, the modified Cahn-Hilliard two-step scheme can inpaint the occluded parts of the writing. The initial value for ε was .08. At $t = 100$, ε was switched to .01. The program was then run to 1000 time steps. Δt was set to 1, the fidelity constant λ was set to 50,000,000, C_1 was set to 10,000, while C_2 was set to 3λ. The final inpainting result is shown in figure 4.6(b).

In figure 4.7(a), graffiti is written over the UCLA logo. Using the graffiti as the inpainting region, the modified Cahn-Hilliard equation inpaints the missing logo parts by the two-step method. Until $t = 50$, a large value of ε ($= .8$) is used. At $t = 50$, ε is switched to a small value ($= .005$). The final result in figure 4.7(b) is the completed logo, looking no worse for wear after its encounter with graffiti. Δt was set to 1, the fidelity constant λ was set to 50,000,000, C_1 was set to 15,000, while C_2 was set to 3λ.

(a) (b)

Figure 4.8: Recovering obscured text. (Image domain is 256×256).

Figure 4.8 shows another example of how the modified Cahn-Hilliard equation can be used to recover obscured text. Figure 4.8(a) shows the text obscured by lines. This is a common problem for Optical Character Recognition (OCR) algorithms, with regard to text written on lined paper. Figure 4.8(b) shows the result after processing by the modified Cahn-Hilliard equation.

The parameters were set as $\Delta t = 1$, $\lambda = 100,000,000$, $C_1 = 10,000$, $C_2 = 3\lambda$, $\varepsilon = .008$, and were kept constant during this particular test. the test was completed at time $t = 800$, which corresponds to 2 minutes of processing time.

4.7 Super-resolution

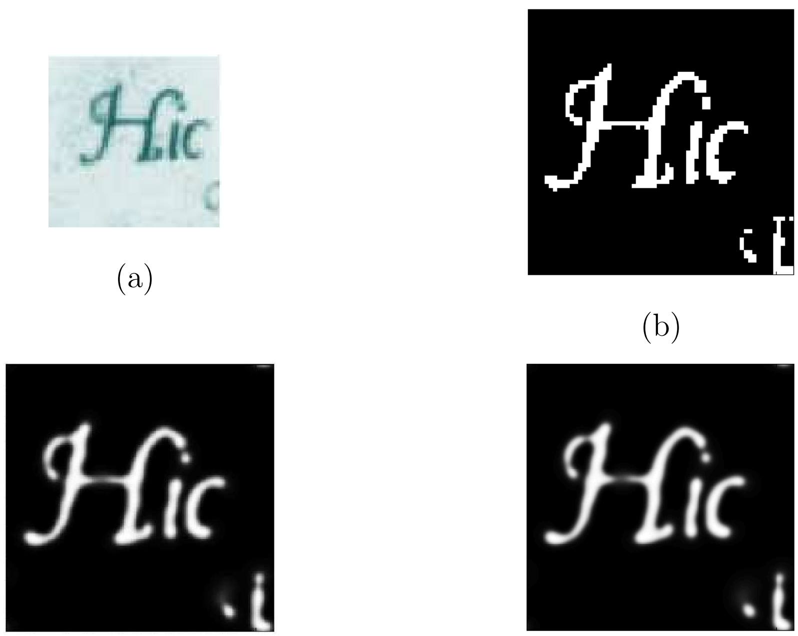

(a) (b) (c) (d)

Figure 4.9: Super-resolution of text. Magnification 3X. (Original size 64×64).

The modified Cahn-Hilliard equation can also be used for the purposes of super-resolution of text. Latin writing is shown in figure 4.9(a), of size 64×64. Figure 4.9(b) shows the text enlarged by 3X using MATLAB's "nearest-neighbor" algorithm.

First, the white region of figure 4.9(b) is subsampled to provide initial data for inpainting. Next, the modified Cahn-Hilliard algorithm runs until $t = 40$ using a very large fidelity constant, $\lambda = 50,000,000$, and very small ε (=.005).

After $t = 40$, λ is set equal to zero, and the ordinary Cahn-Hilliard equation is allowed to run on the text. This allows for the smoothing of jagged parts of the text that appeared after magnification (figure 4.9(b)). Figure 4.9(c) and 4.9(d) show the results at $t = 350$ and $t = 450$ respectively (approximately 5 seconds in real time with the Pentium 4 processor). Throughout this test, C_1 was set to 300, C_2 was set to 150,000,000, and ε was set to .005. This particular test used a constant value of ε.

4.8 Comparison with other methods

One of the chief benefits of using the modified Cahn-Hilliard (mCH) equation to do inpainting are the fast numerical techniques available for its solution. To quantitatively determine how much faster this makes the modified Cahn-Hilliard equation than other binary inpainting techniques, a series of comparison tests were run.

The methods we tested against were the Curvature Driven Diffusion (CDD) inpainting model of Chan and Shen [CS01b], the Euler's Elastica (EE) inpainting model of Chan, Kang, and Shen [CSK02], and the Mumford-Shah-Euler (MSE) inpainting model of Esedoglu and Shen [ES02].

Each method was tested on two examples – inpainting a 3/4 circle, and inpainting a disconnected stripe. All tests were run on the same system described at the start of this chapter (with the exception that the EE method was programmed in C++).

$\frac{3}{4}$ circle | Disconnected stripe

Figure 4.10: Inpainting data for comparison tests. Gray color denotes inpainting regions.

4.9 Graphic results

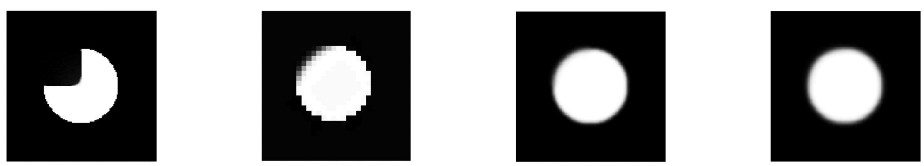

CDD^1 EE^1 MSE^1 mCH^1

CDD^2 EE^2 MSE^2 mCH^2

Figure 4.11: Results for the circle inpainting test. ^{1} – zero initial data assumed in inpainting region. ^{2} – random initial data assumed in inpainting region.

Figures 4.11 and 4.12 show the performance of each inpainting method on the circle and stripe tests, respectively. As can be seen in figure 4.11, CDD requires random data to begin inpainting the circle (CDD^2). The EE method fared well on the circle test with zero initial data in the inpainting region (EE^1), but became mired when the test was started with random data there (EE^2).

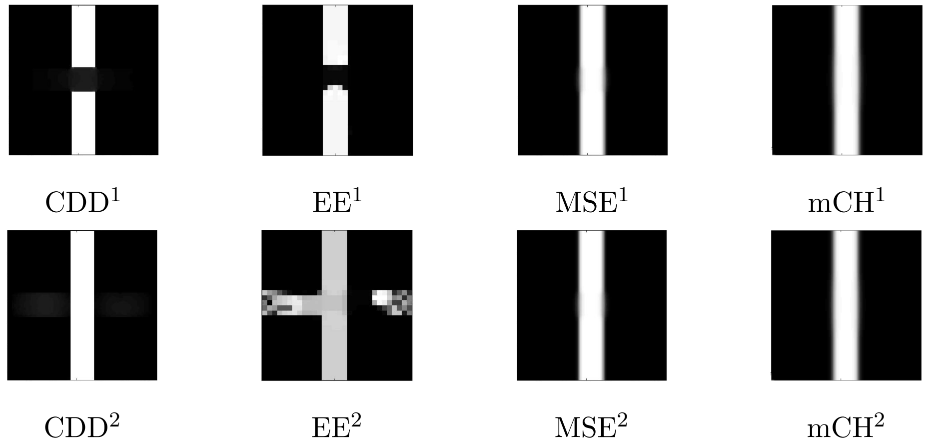

Figure 4.12: Results for the stripe inpainting test. ^{1} – zero initial data assumed in inpainting region. ^{2} – random initial data assumed in inpainting region.

The MSE and mCH methods, however, had no strict preference for the initial data in the inpainting region. Results were the same whether random or zero initial data was assumed (MSE ^{1,2}, mCH ^{1,2}).

Tables 4.1 and 4.2 show the timing results for each method. These are the correct times for the graphical results shown in figures 4.11 and 4.12.

Table 4.1: Comparison tests, inpainting region set to zero data

Method	Inpainting Time (seconds)	
	Circle	Stripe
CDD	$> 5,400$	$> 5,400$
EE*	$> 18,000$	$> 18,000$
MSE	45	24
mCH	24	6

* 30×30 grid used. All others 128×128

Table 4.2: Comparison tests, inpainting region set to random data

Method	Inpainting Time (seconds)	
	Circle	Stripe
CDD	> 270	> 270
EE*	$> 1,800$	$> 1,800$
MSE	300	30
mCH	24	5

* 30×30 grid used. All others 128×128

CHAPTER 5

Future Projects

5.1 Grayscale inpainting using the modified Cahn-Hilliard equation

The chief aim for this project, moving forward, is to extend the inpainting capability of the modified Cahn-Hilliard equation to grayscale images. While binary inpainting can be accomplished handily with our method, grayscale inpainting presents a serious challenge.

The reason for this lies in the use of the double-well potential $W(u)$ contained in the Cahn-Hiliard equation. This double-well worked very well when the only colors of interest were black (one well) and white (the other well). With grayscale we are now interested in 256 colors.

Toward that end, some experiments have been carried out. One idea is to adapt $W(u)$ to have more minima. A simple attempt at this was tried with a $W(u)$ that looked like the following:

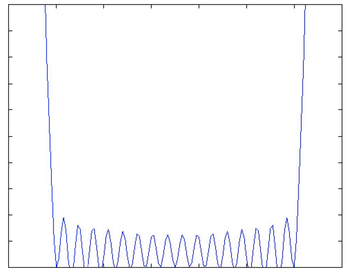

Figure 5.1: A multi-welled $W(u)$ with numerous zeros between $x = 0$ and $x = 1$.

The problem with this particular method is that the minima are not equally spaced relative to each other. This leads to unwanted situations where certain phase transitions are preferred relative to other more physically natural transitions. As a result, this method only provided very basic grayscale inpainting capability, of negligible use. An example is shown below.

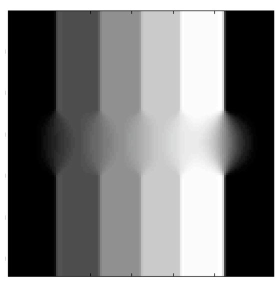

Figure 5.2: A result showing how the modified Cahn-Hilliard with the addtion of a multi-welled $W(u)$ performed.

A more sophisticated treatment of the jump from double-well to multiple-well potentials takes into account the higher dimensions needed to make the minima equidistant from each other. Eyre [Eyr93], among others, has proposed the following energy for the multiphase Cahn-Hilliard equation modeling an alloy composed of $m + 1$ metals:

$$F(w) = \int_{\Omega} \Big(\Phi(w) + \frac{1}{2} tr(\nabla w^T \Gamma \nabla w) \Big) \, dx, \tag{5.1}$$

with the attendant mass-conservation requirement that

$$\frac{1}{|\Omega|}\int_{\Omega} w(x)\ dx = \bar{w}, \tag{5.2}$$

where $\bar{w}$ represents the average of $w(x)$ over Ω, and

$$w \in \Re^m, \quad x \in \Omega \subset \Re^n, \quad t > 0, \quad \Gamma \in \Re^{m\times m}, \quad \Phi : \Re^m \mapsto \Re. \tag{5.3}$$

Equation (5.1) deserves some explanation. The potential $\Phi(w)$ now has $m+1$ wells. The term $\frac{1}{2}tr(\nabla w^T \Gamma \nabla w)$ models a smooth transition between regions of different phase, where Γ is a positive-definite matrix, and "tr" stands for the trace of a matrix, i.e.,

$$tr(A) = \sum_{i=1}^{m} a_{ii}. \tag{5.4}$$

For the purposes of inpainting, the matrix Γ can be assumed to be completely symmetric and constant.

The boundary conditions for (5.1) are then

$$\nabla w \cdot n|_{x\in\partial\Omega} = \nabla \mu \cdot n|_{x\in\partial\Omega} = 0, \tag{5.5}$$

and the variational derivative of (5.1) results in a system of m coupled partial differential equations:

$$\frac{\partial w}{\partial t} = \Delta[-\Gamma\Delta w + \nabla_w \Phi(w)]. \tag{5.6}$$

More detailed information on the structure of the solutions to the multiphase Cahn-Hilliard equation can be found in Eyre [Eyr93].

A drawback to the multiphase approach is the increased computational time needed to compute the solution for grayscale inpainting. For example, for effective grayscale inpainting, 256 "phases" must be used. This means that 255 coupled equations in the form of (5.6) must be solved for each iteration of the inpainting process. This may not be computationally feasible, yet experiments should be attempted to benchmark this method.

Another option might be to use less than the full 256 grayscale colors in the multiphase method, 16 for example, and check if this reduced grayscale inpainting gives passably good results. Especially for the purposes of inpainting, this may be a useful tack.

The work of Scherzer and Grossauer was explained in the introduction of this thesis [GS03]. They have utilized the solution of the complex Ginzburg-Landau equation as a method for grayscale inpainting (see pages 9 and 10 of the introduction for a full explanation). This complex-valued approach was tried for Cahn-Hilliard inpainting. We began with the modified Cahn-Hilliard equation,

$$u_t \;=\; -\Delta\Big(\varepsilon\Delta u - \frac{1}{\varepsilon}W'(u)\Big) + \lambda_0(f \;-\; u)\chi_{\Omega\setminus D}, \tag{5.7}$$

and modified it to now account for $u(x,t) = u_1(x,t) + iu_2(x,t)$:

$$\begin{aligned}\frac{\partial u_1}{\partial t} &= -\Delta\Big(\varepsilon\Delta u_1 - \frac{4}{\varepsilon}\Big[(u_1-\tfrac{1}{2})((u_1-\tfrac{1}{2})^2+u_2^2-\tfrac{1}{4})\Big]\Big) + \lambda_0(f-u_1)\chi_{\Omega\setminus D}\\ \frac{\partial u_2}{\partial t} &= -\Delta\Big(\varepsilon\Delta u_2 - \frac{4}{\varepsilon}\Big[u_2((u_1-\tfrac{1}{2})^2+u_2^2-\tfrac{1}{4})\Big]\Big).\end{aligned} \tag{5.8}$$

As well, we assumed initial values for $u_2(x,t)$ of

$$u_2(x,0) = \sqrt{1-|u_1(x,0)-\tfrac{1}{2}|^2}. \tag{5.9}$$

Some explanation for equation (5.8) is in order. This coupled system can be derived from the energy

$$E(u_1,u_2) = \int_\Omega \frac{\varepsilon}{2}|\nabla u|^2 + \frac{1}{\varepsilon}\Big[(u_1-\tfrac{1}{2})^2+u_2^2-\tfrac{1}{4}\Big]^2\,dx + \int_{\Omega\setminus D}\lambda_0(f-u_1)^2\,dx, \tag{5.10}$$

in the same manner as was demonstrated in chapter 3. However, notice that $W(u)$ has changed to a $W(u_1,u_2)$ which seeks to place the value u_1+iu_2 on the perimeter of a circle of radius 1 centered at $u_1 = \frac{1}{2}$ in the complex u plane.

The rest of (5.10) is nearly the same as it was for the non-complex system for $u(x,t)$ studied earlier. The idea here is that now (we hope), multiple values of u_1 between 0 and 1 can serve as minima for the energy (5.10).

There is much room for experimentation here. For example, one might ask why the imaginary term u_2 needs to be included in the $\frac{\varepsilon}{2}|\nabla u|^2$ term of (5.10). When it is included, a diffusive term appears in the second equation of (5.8), which is of questionable benefit.

As well, notice that only the real term u_1 is accounted for in the fidelity term for the energy (5.10). This would seem to be logical, as we are matching the known image values from outside the inpainting region to u_1, but there is an unknown effect if we were to take $f(x) = f_1(x) + if_2(x)$ with $f_2(x) = \sqrt{1 - |f_1(x) - \frac{1}{2}|^2}$. This is an experiment to try.

CHAPTER 6

Conclusion

We have shown how the Cahn-Hilliard equation can be modified to achieve fast inpainting of binary imagery. This modified Cahn-Hilliard equation can be applied to the inpainting of simple binary shapes, text reparation, road interpolation, and super-resolution. The two-step process we employ, described at the end of section II, allows for effective inpainting across large unknown regions. Although it is generally desired for the end-user to specify the inpainting domain, this method can be used for interpolating simple roads and other situations where a user-defined inpainting region is not feasible.

This method assumes zero data in the inpainting region. The two-step process then channels the solution toward the desired steady state in a repeatable process. Although at least one undesirable steady state may be possible mathematically, the method steers away from this by first achieving a very rough but wide-ranging inpainting, and then using this state as initial data for a subsequent inpainting with sharp transitions between white and black regions.

In the context of binary image inpainting, the modified Cahn-Hilliard equation has displayed a considerable decrease in computation time when compared with other inpainting methods. Fast numerical techniques available for the Cahn-Hilliard equation also allow for larger data sets to be processed, greatly aiding the speed of computation.

References

[ABC94] Nicholas Alikakos, Peter W. Bates, and Xinfu Chen. "Convergence of the Cahn-Hilliard Equation to the Hele-Shaw Model." *Arch. Rational Mech. Anal.*, **128**:165–205, 1994.

[Ada75] R.A. Adams. *Sobolev Spaces.* Academic Press, New York, 1975.

[Arc] Northwestern University Archives. "John E. Hilliard (1926-1986) Papers, 1947-1986.".

[AT90] L. Ambrosio and V. M. Tortorelli. "Approximation of functionals depending on jumps by elliptic functionals via Gamma convergence." *Communications on Pure and Applied Mathematics*, **43**:999–1036, 1990.

[BBC01] C. Ballester, M. Bertalmio, V. Caselles, G. Sapiro, and J. Verdera. "Filling-in by joint interpolation of vector fields and grey levels." *IEEE Transactions on Image Processing*, **10**(8):1200–1211, 2001.

[BBS01] M. Bertalmio, A. Bertozzi, and G. Sapiro. "Navier-Stokes, fluid dynamics, and image and video inpainting." *IEEE Computer Vision and Pattern Recognition (CVPR), Hawaii*, **1**:I355–I362, December 2001.

[BEG06] A. Bertozzi, S. Esedoglu, and A. Gillette. "Analysis of a two-scale Cahn-Hilliard model for image inpainting." *Submitted for publication*, 2006.

[BEGar] A. Bertozzi, S. Esedoglu, and A. Gillette. "Inpainting of Binary Images Using the Cahn-Hilliard Equation." *IEEE Trans. Image Proc.*, to appear.

[Bel97] G. Bellettini. "Variational approximation of functionals with curvatures and related properties." *Journal of Convex Analysis*, **4**(1):91–108, 1997.

[BF93] P. Bates and P. Fife. "The dynamics of nucleation for the Cahn-Hilliard equation." *SIAM J. Appl. Math*, **53(4)**:553–582, 1993.

[BG04] A. L. Bertozzi and J. B. Greer. "Low curvature image simplifiers: global regularity of smooth solutions and Laplacian limiting schemes." *Communications on Pure and Applied Mathematics*, **57**(6):764–790, 2004.

[BMP93] G. Bellettini, G. Dal Maso, and M. Paolini. "Semicontinuity and relaxation properties of a curvature depending functional in 2D." *Ann. Sc. Norm. Sup. Pisa*, **XX**(2):247–299, 1993.

[BP95] G. Bellettini and M. Paolini. "Variational properties of an image segmentation functional depending on contours curvature." *Advances in Mathematical Sciences and Applications*, **5**(2):681–715, 1995.

[Bra98] A. Braides. *Approximation of free-discontinuity problems.* Number 1694 in Lecture Notes in Mathematics. Springer-Verlag, 1998.

[BSC00] M. Bertalmio, G. Sapiro, V. Caselles, and C. Ballester. "Image Inpainting." In Kurt Akeley, editor, *Siggraph 2000, Computer Graphics Proceedings*, pp. 417–424. ACM Press / ACM SIGGRAPH / Addison Wesley Longman, 2000.

[CH58] J.W. Cahn and J.E. Hilliard. "Free energy of a nonuniform system, part I : Interfacial free energy." *J. Chem. Phys. 2*, pp. 258–267, 1958.

[CS01a] T. F. Chan and J. Shen. "Mathematical models of local non-texture inpaintings." *SIAM Journal on Applied Mathematics*, **62**(3):1019–1043, 2001.

[CS01b] T. F. Chan and J. Shen. "Non-texture inpainting by curvature-driven diffusions." *Journal of Visual Communication and Image Representation*, **12**(4):436–449, 2001.

[CSK02] T. Chan, J. Shen, and S. Kang. "Euler's elastica and curvature-based image inpainting." *SIAM Journal on Applied Mathematics*, **63**(2):564–592, 2002.

[DVM02] I. Capuzzo Dolcetta, S. Finzi Vita, and R. March. "Area preserving curve-shortening flows: from phase separation to image processing." *Interfaces and Free Boundaries*, **4**(4):325–343, 2002.

[EM03] S. Esedoglu and R. March. "Segmentation with depth but without detecting junctions." *Journal of Mathematical Imaging and Vision*, **18**:7–15, 2003.

[ES02] S. Esedoglu and J. Shen. "Digital inpainting based on the Mumford-Shah-Euler image model." *European Journal of Applied Mathematics*, **13**:353–370, 2002.

[Eva98] Lawrence C. Evans. *Partial differential equations.* American Mathematical Society, Providence, RI, 1998.

[Eyr93] David Eyre. "Systems of Cahn-Hilliard Equations." *SIAM Journal on Applied Mathematics*, **53**(6):1686–1712, 1993.

[Eyr98] David Eyre. "An Unconditionally Stable One-Step Scheme for Gradient Systems.", Unpublished paper, June 9, 1998.

[Fif00] Paul C. Fife. "Models for phase separation and their mathematics." *Electronic Journal of Differential Equations*, **2000**(48):1–26, 2000.

[Fol95] Gerald B. Folland. *Introduction to partial differential equations.* Princeton University Press, Princeton, NJ, second edition, 1995.

[FU] J. Feldman and G. Uhlmann. *Inverse Problems.* To be published.

[GB04a] J. B. Greer and A. L. Bertozzi. "H^1 solutions of a class of fourth order nonlinear equations for image processing." *Journal of Discrete and Continuous Dynamical Systems*, **10**(1-2):349–366, 2004.

[GB04b] J. B. Greer and A. L. Bertozzi. "Traveling wave solutions of fourth order PDEs for image processing." *SIAM Journal on Mathematical Analysis*, **36**(1):38–68, 2004.

[GBS06] J. B. Greer, A. L. Bertozzi, and G. Sapiro. "Fourth Order Partial Differential Equations on General Geometries." *J. Computational Physics*, **216(1)**:216–246, 2006.

[GG84] S. Geman and D. Geman. "Stochastic Relaxation, Gibbs Distributions, and the Bayesian Restoration of Images." *IEEE Transactions on Pattern Analysis and Machine Intelligence*, **20**(6):721–741, 1984.

[Gio91] E. De Giorgi. "Some remarks on Gamma-convergence and least squares methods." In G. Dal Maso and G. F Dell'Antonio, editors, *Composite Media and Homogenization Theory*, pp. 135–142. Birkhauser, 1991.

[Gla03] Karl Glasner. "A Diffuse Interface approach to Hele-Shaw flow." *Nonlinearity*, **16**:49–66, 2003.

[GS03] H. Grossauer and O. Scherzer. "Using the Complex Ginzburg-Landau, Equation for Digital Inpainting in 2D and 3D." *Scale Space Methods in Computer Vision, Lecture Notes in Computer Science*, **2695**:225–236, 2003.

[GT83] D. Gilbarg and N.S. Trudinger. *Elliptic Partial Differential Equations of Second Order.* Springer-Verlag, Berlin, second edition, 1983.

[Hil70] J. Hilliard. "Spinodal decomposition." *Phase transformations, edited by H. I. Aronson (American Society for Metals, Metals Park, Ohio)*, pp. 497–560, 1970.

[KJV82] S. Kirkpatrick, C. D. Gellatt Jr., and M. P. Vecchi. "Optimization by simulated annealing." *IBM Thomas J. Watson Research Center, Yorktown Heights, NY*, 1982.

[LKK05] H.-W. Lu, A. L. Bertozzi K. Glasner, and C.-J. Kim. "A Diffuse Interface Model for Electrowetting Droplets in a Hele-Shaw Cell." *Submitted for publication*, 2005.

[LL86] L. D. Landau and E. M. Lifshitz. *Theory of elasticity.* Butterworth-Heinemann, 1986.

[Mas93] G. Dal Maso. *An Introduction to Gamma Convergence.* Number 8 in Progress in Nonlinear Differential Equations and their Applications. Birkhauser, 1993.

[MD97] R. March and M. Dozio. "A variational method for the recovery of smooth boundaries." *Image and Vision Computing*, **15**(9):705–712, 1997.

[MM77] L. Modica and S. Mortola. "Un esempio di Gamma-convergenza." *Boll. Un. Mat. Ital. B (5)*, **14**(1):285–299, 1977.

[MM98] S. Masnou and J.M. Morel. "Image restoration involving connectedness." *Workshop on Digital Image Processing and Computer Graphics, Vienna, Austria, SPIE*, **3346**, 1998.

[MS63] W. W. Mullins and R. F. Sekerka. "Morphological Stability of a Particle Growing by Diffusion or Heat Flow." *Journal of Applied Physics*, **34**(2):323–329, 1963.

[MS89] D. Mumford and J. Shah. "Optimal approximations by piecewise smooth functions and associated variational problems." *Communications on Pure and Applied Mathematics*, **42**(8):577–685, 1989.

[MS95] J. M. Morel and S. Solimini. *Variational Methods in Image Segmentation.* Progress in Nonlinear Differential Equations and their Applications. Birkhauser, 1995.

[NMS93] M. Nitzberg, D. Mumford, and T. Shiota. *Filtering, Segmentation, and Depth.* Number 662 in Lecture Notes in Computer Science. Springer-Verlag, 1993.

[NS84] A. Novick-Cohen and L. A. Segal. "Nonlinear Aspects of the Cahn-Hilliard Equation." *Physica D*, **10**(3):277–298, 1984.

[OR90] S. Osher and L. Rudin. "Feature oriented image enhancement using shock filters." *SIAM J. Num. Anal.*, **27**(4):919–940, 1990.

[Peg89] R. Pego. "Front migration in the nonlinear Cahn-Hilliard equation." *Proc. Roy. Soc. London A*, **422**(1863):261–278, 1989.

[PM90] P. Perona and J. Malik. "Scale-space and edge detection using anisotropic diffusion." *IEEE Transactions on Pattern Analysis and Machine Intelligence*, **12**(7):629–639, 1990.

[RO94] L. Rudin and S. Osher. "Total variation based image restoration with free local constraints." In *Proc IEEE ICIP, Austin*, volume 1, pp. 31–35, November 1994.

[ROF92] L. Rudin, S. Osher, and E. Fatemi. "Nonlinear total variation based noise removal algorithms." *Physica D*, **60**(1-4):259–268, 1992.

[RT71] A. Rosenfeld and M. Thurston. "Edge and curve detection for visual scene analysis." *IEEE Trans. Comput.*, **C-20**:562–569, 1971.

[SGS03] A. Shindler, M.F. Gyurer, G.D. Simms, D.D. Vvendensky, R.E. Caflisch, C. Connel, and E. Luo. "Theory of strain relaxation in heteroepitaxial systems." *Physical Review B*, **67**(075316), 2003.

[She03] J. Shen. "Inpainting and The Fundamental Problem of Image Processing." *SIAM News*, **36**(5), 2003.

[Str89] J. Strikwerda. *Finite Difference Schemes and Partial Differential Equations*. Wadsworth and Brooks/Cole Advanced Books and Software, 1989.

[Str94] S. H. Strogatz. *Nonlinear dynamics and chaos: With applications to physics, biology, chemistry, and engineering.* Perseus Books, Cambridge MA., 1994.

[TC94] J. E. Taylor and J. W. Cahn. "Linking anisotropic sharp and diffuse surface motion laws via gradient flows." *J. Stat. Phys.*, **77**(1-2):183–197, 1994.

[Tem97] Roger Temam. *Infinite-Dimensional Dynamical Systems in Mechanics and Physics*. Springer-Verlag, New York, New York, second edition, 1997.

[VR03] B. P. Vollmayr-Lee and A. D. Rutenberg. "Fast and accurate coarsening simulation with an unconditionally stable time step." *Physical Review E*, **68**(0066703):1–13, 2003.

[Wal04] Sarah Walden. *The Ravished Image: an introduction to the art of picture restoration and its risks.* Lecture Notes in Mathematics. London: Gibson Square, 2004.

[Wei74] R. Weinstock. *Calculus of Variations.* Dover, 1974.

[YP86] A. Yuille and T. Poggio. "Scaling theorems for zero crossings." *IEEE Transactions on Pattern Analysis and Machine Intelligence*, **PAM1-8**:15–25, 1986.